AIAA

NASA/CR - 1998 - 207286

067583
(C)(UNIV)

AIAA 98-0283

Numerical Simulation of the Generation of Axisymmetric Mode Jet Screech Tones

H. Shen and C. K. W. Tam
Florida State University
Tallahassee, FL

36th Aerospace Sciences Meeting & Exhibit
January 12–15, 1998 / Reno, NV

NUMERICAL SIMULATION OF THE GENERATION OF AXISYMMETRIC MODE JET SCREECH TONES[†]

Hao Shen[*] and Christopher K.W. Tam[**]
Florida State University
Tallahassee, FL 32306-3027

Abstract

An imperfectly expanded supersonic jet, invariably, radiates both broadband noise and discrete frequency sound called screech tones. Screech tones are known to be generated by a feedback loop driven by the large scale instability waves of the jet flow. Inside the jet plume is a quasi-periodic shock cell structure. The interaction of the instability waves and the shock cell structure, as the former propagates through the latter, is responsible for the generation of the tones. Presently, there are formulas that can predict the tone frequency fairly accurately. However, there is no known way to predict the screech tone intensity. In this work, the screech phenomenon of an axisymmetric jet at low supersonic Mach number is reproduced by numerical simulation. The computed mean velocity profiles and the shock cell pressure distribution of the jet are found to be in good agreement with experimental measurements. The same is true with the simulated screech frequency. Calculated screech tone intensity and directivity at selected jet Mach number are reported in this paper. The present results demonstrate that numerical simulation using computational aeroacoustics methods offers not only a reliable way to determine the screech tone intensity and directivity but also an opportunity to study the physics and detailed mechanisms of the phenomenon by an entirely new approach.

1. Introduction

Supersonic jet noise consists of three principal components[1]. They are the turbulent mixing noise, the broadband shock associated noise and the screech tones. Screech tones are discrete frequency sound. At low supersonic Mach number, the screech tones are associated with the axisymmetric oscillations of the jet and radiate principally in the upstream direction. It has been known since the early work of Powell[2] that screech tones are generated by a feedback loop. Recent works[1] suggest that the feedback loop is driven by the instability waves of the jet flow. In the plume of an imperfectly expanded jet is a quasi-periodic shock cell structure. Figure 1 shows schematically the feedback loop. Near the nozzle lip where the jet mixing layer is thin and most receptive to external excitation, acoustic disturbances impinging on this area excite the instability waves. The excited instability waves, extracting energy from the mean flow, grow rapidly as they propagate downstream. After propagating a distance of four to five shock cells, the instability wave having acquired a large enough amplitude interacts with the quasi-periodic shock cells in the jet plume. The unsteady interaction generates acoustic radiation, part of which propagates upstream outside the jet. Upon reaching the nozzle lip region, they excite the mixing layer of the jet. This leads to the generation of new instability waves. In this way, the feedback loop is closed.

At the present time, there are reliable screech tone frequency prediction formulas[1,3]. However, there is no known way to predict tone intensity and directivity; even if it is entirely empirical. This is not surprising for the tone intensity is determined by the nonlinearities of the feedback loop.

The principle objective of the present work is to simulate the screech phenomenon numerically for low supersonic Mach number jets. It will be shown that numerical simulation is an accurate method for screech tone intensity and directivity prediction. Numerical simulation of jet noise generation is not a straightforward undertaking. Tam[4] had earlier discussed some of the major computational difficulties anticipated in such an effort. First of all, the problem is characterized by very disparate length scales. For instance, the acoustic wavelength of the screech tone is over 20 times larger than the initial thickness of the jet mixing layer that supports the instability waves. Further, there is also a large disparity between the magnitude of the velocity of the radiated sound and that of the jet flow. Typically, they are five to six orders different. To be able to compute accurately the instability waves and the radiated sound, a highly accurate computational aeroacoustics algorithm with shock capturing capability as well as a set of high quality numerical boundary conditions are required.

---

[*] Graduate student, Department of Mathematics.

[**] Distinguished Research Professor, Department of Mathematics. Associate Fellow AIAA.

The rest of this paper is as follows. In Section 2, the mathematical model, the computation algorithm and grid design are discussed. Section 3 describes the various numerical boundary conditions used in the simulation. Section 4 elaborates on the distribution of artificial selective damping incorporated in the computation algorithm. The artificial selective damping terms are for the elimination of the high wavenumber spurious waves. They have no effect on the low wavenumber component (the physical solution) of the computation. They help to maintain a high quality numerical solution free from contamination by spurious waves and numerical instability. Comparisons between numerical results and experimental measurements are provided in Section 5. These include the mean velocity profiles, the shock cell structure, the dependence of the screech tone frequency on jet Mach number and screech tone intensity. Excellent agreements with experimental measurements are found. Computed directivities for the first two harmonics of the dominant screech tone will also be provided.

2. Mathematical Model, Computation Scheme and Grid Design

In this work, we are interested in simulating the axisymmetric mode jet screech in the jet Mach number range of 1.0 to 1.25. The axisymmetric mode is the dominant screech mode for axisymmetric jets from convergent nozzles at these Mach numbers. For this purpose, only two dimensional computation in the $x - r$ plane, where (r, θ, x) are the cylindrical coordinates, are necessary.

2.1. The Mathematical Model

For an accurate simulation of jet screech generation, it is essential that the feedback loop be modeled and computed correctly. The important elements that form the feedback loop are the shock cell structure, the large scale instability wave, and the feedback acoustic waves. Since turbulence in the jet plays only an indirect role in the feedback loop, no attempt is made here to resolve it computationally. However, turbulence in the mixing layer of the jet is responsible for its spreading and the spreading rate of the jet affects the spatial growth and decay of the instability wave. To ensure a good simulation of the spreading rate, the $k - \varepsilon$ turbulence model is adopted. In the computation, the modified $k - \varepsilon$ of Ref. [5], optimized for jet flows, are used.

Figure 2 shows the physical domain to be simulated. We will use length scale $= D$ (nozzle exit diameter), velocity scale $= a_\infty$ (ambient sound speed), time scale $= \frac{D}{a_\infty}$, density scale $= \rho_\infty$ (ambient gas

density), pressure scale $= \rho_\infty a_\infty^2$, temperature scale $= T_\infty$ (ambient gas temperature); scales for k, ε and ν_t are a_∞^2, $\frac{a_\infty^3}{D}$ and $a_\infty D$, respectively. The dimensionless governing equations in Cartesian tensor notation are,

$$\frac{\partial \bar{\rho}}{\partial t} + \frac{\partial \bar{\rho} \tilde{u}_j}{\partial x_j} = 0 \tag{1}$$

$$\frac{\partial \bar{\rho} \tilde{u}_i}{\partial t} + \frac{\partial}{\partial x_j} (\bar{\rho} \tilde{u}_i \tilde{u}_j) = -\frac{\partial \bar{p}}{\partial x_i} - \frac{\partial}{\partial x_j} (\bar{p} \tau_{ij}) \tag{2}$$

$$\frac{\partial \bar{\rho} E}{\partial t} + \frac{\partial}{\partial x_j} (\bar{\rho} E \tilde{u}_j) = -\frac{\partial}{\partial x_j} (\bar{p} \tilde{u}_j)$$

$$- \frac{\partial}{\partial x_j} (\bar{p} \tilde{u}_i \tau_{ij}) + \frac{1}{P_r (\gamma - 1)} \frac{\partial}{\partial x_j} \left(\bar{\rho} \nu_t \frac{\partial \tilde{T}}{\partial x_j} \right)$$

$$+ \frac{1}{\sigma_k} \frac{\partial}{\partial x_j} \left(\bar{\rho} \nu_t \frac{\partial k}{\partial x_j} \right) \tag{3}$$

$$\frac{\partial \bar{\rho} k}{\partial t} + \frac{\partial}{\partial x_j} (\bar{\rho} k \tilde{u}_j) = -\bar{\rho} \tau_{ij} \frac{\partial \tilde{u}_i}{\partial x_j} - \bar{\rho} \varepsilon$$

$$+ \frac{1}{\sigma_k} \frac{\partial}{\partial x_j} \left(\bar{\rho} \nu_t \frac{\partial k}{\partial x_j} \right) \tag{4}$$

$$\frac{\partial \bar{\rho} \varepsilon}{\partial t} + \frac{\partial}{\partial x_j} (\bar{\rho} \varepsilon \tilde{u}_j) = -C_{\varepsilon 1} \frac{\varepsilon}{(k + k_0)} \bar{\rho} \tau_{ij} \frac{\partial \tilde{u}_i}{\partial x_j}$$

$$- C_{\varepsilon 2} \frac{\bar{\rho} \varepsilon^2}{(k + k_0)} + \frac{1}{\sigma_\varepsilon} \frac{\partial}{\partial x_j} \left(\bar{\rho} \nu_t \frac{\partial \varepsilon}{\partial x_j} \right) \tag{5}$$

$$\gamma \bar{p} = \bar{\rho} \tilde{T} \tag{6}$$

$$E = \frac{\tilde{T}}{\gamma (\gamma - 1)} + \frac{1}{2} \tilde{u}_i^2 + k \tag{7}$$

$$\tau_{ij} = \frac{2}{3} k \delta_{ij} - \nu_t \left(\frac{\partial \tilde{u}_i}{\partial x_j} + \frac{\partial \tilde{u}_j}{\partial x_i} - \frac{2}{3} \frac{\partial \tilde{u}_k}{\partial x_k} \delta_{ij} \right) \tag{8}$$

$$\nu_t = C_\mu \frac{k^2}{(\varepsilon + \varepsilon_0)} + \frac{\nu}{a_\infty D} \tag{9}$$

where γ is the ratio of specific heats, ν is the molecular kinematic viscosity. $k_0 = 10^{-6}$ and $\varepsilon_0 = 10^{-4}$ are small positive numbers to prevent the division by zero. The model constants are taken to be[5],

$$C_\mu = 0.0874, \quad \sigma_k = 0.324, \quad \sigma_\varepsilon = 0.377,$$
$$C_{\varepsilon 1} = 1.4, \quad C_{\varepsilon 2} = 2.02, \quad P_r = 0.422,$$
$$\frac{\nu}{a_\infty D} = 1.7 \times 10^{-6}.$$

It is to be noted that for the range of Mach number and jet temperature considered the Pope and Sarkar corrections often added to the $k - \varepsilon$ model[5] are not necessary. Outside the jet flow both k and ε are zero. On neglecting the molecular viscosity terms, the governing equations become the Euler equations.

In this work, solutions of the above set of equations are to be found numerically. For a given jet

2

operating condition, the solution is to provide the shock cell structure in the jet plume, the mean flow as well as the instability wave in the mixing layer and the acoustic field of the screech tone outside the jet.

2.2. Computation scheme and grid design

In this work, the 7-point stencil DRP scheme[4,6] is used to time-march the solution to a time periodic state corresponding to the screech cycle. The coefficients of the scheme including those of the backward difference stencils are given in Ref [4] (the value of a_3 should be 0.0208431427703). The DRP scheme has proven to be nearly nondispersive over a wide band of wavenumbers. In the acoustic region, the use of 8 mesh points per wavelength would be adequate. This allows a fairly coarse grid to be used in the entire region outside the jet flow.

2.3. Grid Design

The mixing layer of the jet is very thin. The smallest size grid is employed here to provide needed resolution. Figure 3 shows the entire computation domain. The domain extends 5 diameters back from the nozzle exit and 35 diameters long in the x-direction. It is 17 diameters in the r-direction. The domain is divided into four blocks (or subdomains) as far as the grid size is concerned. In Figure 3, these subdomains are separated by black lines. The black lines represent buffer regions of 3 mesh spacings. Since acoustic waves propagate with no preference in direction, square grids are used. The finest grid in the block right downstream of the nozzle exit has $\Delta x = \frac{D}{64}$. This block is enclosed by the next block with $\Delta x = \frac{D}{32}$ which, in turn, is enclosed by another block with $\Delta x = \frac{D}{16}$. The outer most block has $\Delta x = \frac{D}{8}$. In Figure 3, the dotted curve represents more or less the edge of the jet flow. This is well inside the lightly shaded region in which the governing equations are the $k - \varepsilon$ model turbulent flow equations. The full Euler equations are used in the unshaded region.

The buffer region is a narrow region around the boundaries of a computation subdomain of uniform size mesh. The change in the mesh size takes place in the buffer region. The basic design of the buffer region can be found in Ref [7]. In this work, a slightly improved version of the basic design is used.

3. Numerical Boundary Conditions

Numerical boundary conditions play a crucial role in the simulation of the jet screech phenomenon. Recently an in-depth review of this subject was given by Tam[8]. For the present problem, several types of numerical boundary conditions are required. In Figure 2, outflow boundary conditions are necessary along boundary AB. Along boundary $BCDE$, radiation condition with entrainment flow are required. On the nozzle wall, the solid wall boundary condition is imposed. The jet flow is supersonic. So the inflow boundary condition can be prescribed at the nozzle exit plane. Finally, the equations of motion in cylindrical coordinates centered on the x-axis have an apparent singularity at the jet axis ($r \rightarrow 0$). A special treatment is needed to avoid the singularity computationally. Below, a brief description of the different boundary conditions used in the simulations is provided.

3.1. Radiation Boundary Conditions with Entrainment Flow

For accurate numerical simulation, the numerical boundary conditions to be imposed along boundary $BCDE$ must perform three functions. First, it must specify the ambient conditions for the entire computation. This information is critical to the correct expansion of the jet and the development of the shock cell structure. Second, it must allow the acoustic waves generated to leave the computation domain with minimal reflection. Third, it must generate the entrainment flow induced by the jet. The development of such a set of radiation boundary conditions with entrainment flow is discussed in Ref [8].

3.2. Outflow Boundary Conditions

Along the outflow boundary AB, the mean flow is nonuniform. For this reason, the nonuniform outflow boundary conditions of Tam and Dong[9] is used. However, as the outflow boundary is only 30 jet diameters downstream, the instability wave amplitude, although damped at such a far distance, remains quite large. To allow for weak nonlinearities, we nonlinearized the outflow boundary conditions of Tam and Dong by replacing the linear terms by their nonlinear counterparts. In cylindrical coordinates, the complete set of outflow boundary conditions used are,

$$\frac{\partial \rho}{\partial t} + u\frac{\partial \rho}{\partial x} + v\frac{\partial \rho}{\partial r} = \frac{1}{a^2}\left(\frac{\partial p}{\partial t} + u\frac{\partial p}{\partial x} + v\frac{\partial p}{\partial r}\right) \tag{10}$$

$$\frac{\partial u}{\partial t} + u\frac{\partial u}{\partial x} + v\frac{\partial u}{\partial r} = -\frac{1}{\rho}\frac{\partial p}{\partial x} \tag{11}$$

$$\frac{\partial v}{\partial t} + u\frac{\partial v}{\partial x} + v\frac{\partial v}{\partial r} = -\frac{1}{\rho}\frac{\partial p}{\partial r} \tag{12}$$

$$\frac{1}{V(\theta)}\frac{\partial p}{\partial t} + \cos\theta\frac{\partial p}{\partial x} + \sin\theta\frac{\partial p}{\partial r} + \frac{p - \overline{p}}{R} = 0 \tag{13}$$

3

$$\frac{\partial k}{\partial t} + u\frac{\partial k}{\partial x} + v\frac{\partial k}{\partial r} = 0 \qquad (14)$$

$$\frac{\partial \varepsilon}{\partial t} + u\frac{\partial \varepsilon}{\partial x} + v\frac{\partial \varepsilon}{\partial r} = 0 \qquad (15)$$

where $V(\theta) = u\cos\theta + a(1 - M^2\sin^2\theta)^{\frac{1}{2}}$, $M = \frac{u}{a}$. a is the speed of sound and (θ, R) are spherical polar coordinates (the x-axis is the polar axis); the origin of R has been taken to be at the end of the potential core of the jet. The last two equations above are the nonlinearized form of the linear asymptotic $k - \varepsilon$ equations (without sources). $\bar{p}$ is the static pressure calculated by the entrainment flow model at the edge of the jet flow at the outflow boundary.

3.3. Inflow Boundary Conditions

At the nozzle exit plane, the flow variables are taken to be uniform corresponding to those at the exit of a convergent nozzle. In addition, both k and ε are assumed to be zero. In other words, the mixing layer is regarded to be very thin. Thies and Tam[5], in their jet mean flow calculation work, found that this is a reasonably good way to initiate the computation. For cold jets, the mixing layer evolves rapidly into a quasi-similar state resembling that in a physical experiment.

3.4. Boundedness Treatment at the Jet Axis

In cylindrical coordinates, the governing equation has an apparent singularity at the jet axis ($r \rightarrow 0$). Ref [8] discusses two ways to treat this problem. In the present work, the governing equations are not used at $r = 0$. Instead, the formal limit of these equations as $r \rightarrow 0$ are used. Our experience is that this can be implemented in a straightforward manner by extending the 7-point stencil into the negative region of r. The flow variables ρ, p and u in the $r < 0$ region are determined by symmetric extension about the jet axis while v is obtained by an antisymmetric extension. These are the proper extensions for axisymmetric jet screech oscillations.

3.5. Wall Boundary Conditions

On the nozzle wall, the boundary condition of no through flow is implemented by the ghost point method of Tam and Dong[10]. For the purpose of eliminating the generation of spurious waves, extra amounts of artificial selective damping are imposed around the nozzle wall region. By judging from the computed results, this is an effective way to avoid the generation of short spurious waves.

4. Artificial Selective Damping

The DRP scheme is a central difference scheme and, therefore, has no intrinsic dissipation. For the purpose of eliminating spurious short waves and to improve numerical stability, artificial selective damping terms[11] are added to the discretized finite difference equations.

In the interior region, the seven-point damping stencil[4] (with half-width $\sigma = 0.2\pi$) is used. An inverse mesh Reynolds number ($R_\Delta^{-1} = \frac{\nu_a}{(a_\infty \Delta x)}$ where ν_a is the artificial kinematic viscosity) of 0.05 is prescribed over the entire computation domain. This is to provide general background damping to eliminate possible propagating spurious waves. Near the boundaries of the computation domain where a 7 points stencil does not fit, the 5 and 3 points damping stencils given in Ref. [4] are used.

Spurious numerical waves are usually generated at the boundaries of a computation domain. The boundaries are also favorite sites for the occurrence of numerical instability. This is true for both exterior boundaries as well as internal boundaries such as the nozzle walls and buffer regions where there is a change in mesh size. To suppress both the generation of spurious numerical waves and numerical instability, additional artificial selective damping is imposed along these boundaries. Along the inflow (radiation) and outflow boundaries, a distribution of inverse mesh Reynolds number in the form of a Gaussian function with a half-width of 4 mesh points (normal to the boundary) and a maximum value of 0.1 right at the outermost mesh points is incorporated into the time marching scheme. Adjacent to the jet axis, a similar addition of artificial selective damping is implemented with a maximum value of the inverse mesh Reynolds number at the jet axis set equal to 0.35. On the nozzle wall, the use of a maximum value of additional inverse mesh Reynolds number of 0.2 has been found to be very satisfactory.

The two sharp corners of the nozzle lip and the transition point between the use of the outflow and the radiation boundary condition on the right side of the computation domain are locations requiring further additional numerical damping. This is done by adding a Gaussian distribution of damping around these special points.

As shown in figure 3, the four computation subdomains are separated by buffer regions. Here additional artificial selective damping is added to the finite difference scheme. In the supersonic region downstream of the nozzle exit, a shock cell structure develops in the jet flow. In order to provide the DRP scheme with shock capturing capability, the variable stencil Reynolds number method of Tam and Shen[12] is adopted. The jet mixing layer in this region has very large velocity gradient in the radial direction.

4

Because of this, the $U_{stencil}$ of the variable stencil Reynolds number method is determined by searching over the seven-point stencil in the axial direction and only the two immediately adjacent mesh points in the radial direction. An inverse stencil Reynolds number distribution of the form,

$$R^{-1}_{stencil} = 4.5F(x)G(r) \qquad (16)$$

where

$$F(x) = \begin{cases} 1, & 0 \le x \le 9 \\ \exp[-\frac{\ell n\,2}{(8\Delta x)^2}(x-9)^2], & 9 < x \end{cases}$$

$$G(r) = \begin{cases} 1, & 0 \le r \le 0.8 \\ \exp[-\frac{\ell n\,2}{(4\Delta x)^2}(r-0.8)^2], & 0.8 < r \end{cases}$$

is used in all numerical simulations. It is possible to show, based on the damping curve ($\sigma = 0.3\pi$) that the variable damping has minimal effect on the instability wave of the feedback loop. Also extensive numerical experimentations indicate that the method used can, indeed, capture the oscillatory shocks in the jet plume and that the time averaged shock cell structure compares favorably with experimental measurements.

5. Numerical Results and Comparisons with Experiments

We have been able, using the numerical algorithm described above, to reproduce the jet screech phenomenon computationally. Figure 4 shows the computed density field in the $x - r$-plane at one instance after the initial transient disturbances have propagated out of the computational domain. The screech feedback loop locks itself into a periodic cycle without external interference. As can be seen, sound waves of the screech tones are radiated out in a region around the fourth to fifth shock cells downstream of the nozzle exit. Most of the prominent features of the numerically simulated jet screech phenomenon are in good agreement with physical experiments[13,14,15].

5.1. Mean Velocity Profiles and Shock Cell Structure

To demonstrate that the present numerical simulation can actually reproduce the physical experiment, we will first compare the mean flow velocity profile of the simulated jet with experimental measurements. For this purpose, the time averaged velocity profile of the axial velocity of a Mach 1.2 jet from 1 diameter downstream of the nozzle exit to 7 diameters downstream at one diameter interval are measured from the numerical simulation. They are shown as a function of $\eta^* = \frac{(r-r_{0.5})}{x}$ in figure 5 where $r_{0.5}$ is the radial distance from the jet axis to the location where the axial velocity is equal to half the fully expanded jet velocity. Numerous experimental measurements have shown that the mean velocity profile when plotted as a function of η^* would nearly collapse into a single curve. The single curve is well represented by an error function in the form,

$$\frac{u}{u_j} = 0.5[1 - \mathrm{erf}(\sigma\eta^*)] \qquad (17)$$

where σ is the spreading parameter. Extensive jet mean flow data had been measured by Lau[16]. By interpolating the data of Lau to Mach 1.2, it is found that experimentally σ is nearly equal to 17.0. The empirical fit, formula (17), with $\sigma = 17.0$ is also plotted in figure 5 (the circles). As can readily be seen, there is good agreement between the empirical mean velocity profile and those of the numerical simulation.

One important component of the screech feedback loop is the shock cell structure inside the jet plume. To ensure that the simulated shock cells are the same as those in an actual experiment, we compare the time averaged pressure distribution along the centerline of the simulated jet at Mach 1.2 with the experimental measurements of Norum and Brown [17]. Figure 6 is a plot of the simulated and measured pressure distribution as a function of downstream distance. It is clear from this figure that the first five shocks of the simulation are in good agreement with experimental measurements both in terms of shock cell spacing and amplitude. Beyond the fifth shock cell, the agreement is less good. At this time, we are unable to determine the cause of the discrepancy. However, it is known that screech tones are generated around the fourth shock cell. Therefore, any minor discrepancies downstream of the fifth shock cell would not invalidate our screech tone simulation.

During a screech cycle, the shock cell is not stationary. In the past, Westley and Woolley[13] had made extensive high speed stroboscopic schlieren observations of the motion of the shock cells and the disturbances/instability wave in the mixing layer of the jet. Figure 7a is their hand sketch of the prominent features inside the jet plume. Figure 7b is the density field in a plane cutting through the centerline of the simulated jet. In comparing figures 7a and 7b one must be aware that the lighting in schlieren observation gives an integrated view of the density field across the jet. Despite this inherent difference, there are remarkable similarities between the two fig-

ures. Not only the gross features of the large tur-
bulence structure (in the form of toroidal vortices)
and shock cells are alike, the detailed features of the
curved shocks are nearly the same. Based on the
above comparisons, it is believed that the numerical
simulation, indeed, can reproduce all the important
elements of the screech phenomenon.

5.2. Screech Tone Frequency and Intensity

It is well known that at low supersonic jet Mach
number, there are two axisymmetric screech modes;
the A_1 and the A_2 modes. Earlier, Norum[14] had
compared the frequencies of the A_1 and A_2 modes
measured by a number of investigators. His com-
parison indicates that the screech frequencies and
the Mach number at which the transition from one
mode to the other takes place (staging) vary slightly
from experiment to experiment. It is generally
agreed among experimentalists that the screech phe-
nomenon is extremely sensitive to minor details of
the experimental facility and jet operating condi-
tions.

In the present numerical simulation, both the A_1
and A_2 axisymmetric screech modes are reproduced.
Figure 8 shows the variation of $\frac{\lambda}{D}$, where λ is the
acoustic wavelength of the tone, with jet Mach num-
ber obtained by the present numerical simulation.
Since $\frac{\lambda}{D} = \frac{a_\infty}{(fD)}$, where f is the screech frequency,
this figure essentially provides the frequency Mach
number relationship. Plotted on this figure also are
the measurements of Ponton and Seiner[15]. The data
from both the numerical simulation and experiment
fall on the same two curves, one for the A_1 mode and
the other for the A_2 mode. This suggests that the
calculated screech frequencies are in complete agree-
ment with experimental measurements; although the
Mach number at which staging takes place is not the
same.

Ponton and Seiner[15] mounted two pressure trans-
ducers at a radial distance of $0.642D$ and $0.889D$,
respectively, on the surface of the nozzle lip in their
experiment. By means of these transducers, they
were able to measure the intensities of the screech
tones. Their measured values are plotted in figures
9a and 9b. The transducer of figure 9b is closer
to the jet axis and hence shows a higher dB level.
Plotted on these figures also are the corresponding
tone intensities measured in the numerical simula-
tion. The peak levels of both physical and numerical
experiments are nearly equal. Thus, except for the
difference in the staging Mach number, the present
numerical simulation is, indeed, capable of providing
accurate screech tone intensity prediction as well.

5.3. Directivity

The directivity patterns of the simulated screech
tones have been measured. Typical directivities for
the A_1 and A_2 modes are shown in figures 10 and
11. A search over the literature fails to find directiv-
ity measurements for the axisymmetric mode screech
tones. Validation of these results, therefore, cannot
be carried out at this time.

Figure 10a shows the directivity of the A_1 screech
mode (fundamental frequency) at jet Mach number
1.18 scaled to a distance of $65D$. The directivity of
the second harmonic is given in figure 10b. Those
for the A_2 mode at Mach 1.2 are shown in figures
11a and 11b. Overall, the directivity patterns of the
A_1 and A_2 modes are similar. However, there are
differences in detailed features. For the fundamen-
tal tone, the directivity pattern consists of two prin-
cipal lobes. One lobe radiates upstream and form
part of the screech feedback loop. The other radi-
ates downstream peaked at a relatively small angle
from the jet flow direction. This is not sound gener-
ated by the interaction of instability wave and shock
cells. It is Mach wave radiation generated directly
by the instability wave as it propagates down the jet
column[1,18].

The directivity pattern of the second harmonic,
figures 10b and 11b, also displays two principal
lobes. One lobe peaks around the 90 deg. direction.
This is the principal lobe. The sound is generated by
the nonlinearities of the source (nonlinear instabil-
ity wave shock cell interaction). The other lobe is in
the upstream direction. We believe this is generated
by the nonlinear propagation effect of the upstream
propagating feedback acoustic waves. The screech
tone intensity is quite high. This leads immediately
to wave steepening and the generation of harmon-
ics. An examination of the waveforms measured at
upstream locations confirms that they are not sinu-
soidal but somewhat distorted. Thus the main lobes
of the second harmonic are of entirely different ori-
gin.

Concluding Remarks

Recently, rapid advances have been made in the
development of computational aeroacoustic meth-
ods. In this work, we have demonstrated that it is
now possible to perform accurate numerical simula-
tion of the jet screech phenomenon by the use of one
of these methods, namely, the DRP scheme with ar-
tificial selective damping. Numerical boundary con-
ditions are also crucial to the success of the simula-
tions. At the present time, such numerical boundary
conditions are available in the literature. In a pre-

vious review[4], it was pointed out, unlike traditional computational fluid dynamics problems, numerical simulation of jet noise generation is subjected to the difficulties of large length scale disparity and the need to resolve the many orders of magnitude differences in sound and flow. This work indicates that these problems can be overcome by a careful design of the computation grid and the use of an optimized high order finite difference scheme.

The present work is restricted to the low supersonic Mach number range for which the screech tones are axisymmetric. Future plans call for the extension of the work to three dimensions to allow the simulation of flapping modes at higher Mach numbers.

Acknowledgment

References

1. Tam, C.K.W., "Supersonic Jet Noise," Annual Review of Fluid Mechanics, Vol. 27, 1995, pp. 17–43.
2. Powell, A., "On the Mechanism of Choked Jet Noise," Proceedings Physical Society, London, Vol. 66, 1953, pp. 1039–1056.
3. Tam, C.K.W., Shen, H. and Raman, G., "Screech Tones of Supersonic Jets from Bevelled Rectangular Nozzles," AIAA Journal, Vol. 35, July 1997, pp. 1119–1125.
4. Tam, C.K.W., "Computational Aeroacoustics: Issues and Methods," AIAA Journal, Vol. 33, Oct. 1995, pp. 1788–1796.
5. Thies, A.T. and Tam C.K.W., "Computation of Turbulent Axisymmetric and Nonaxisymmetric Jet Flows Using the $k - \varepsilon$ Model", AIAA Journal, Vol. 34, Feb. 1996, pp. 309–316.
6. Tam, C.K.W. and Webb, J.C., "Dispersion-Relation-Preserving Finite Difference Schemes for Computational Acoustics," Journal of Computational Physics, Vol. 107, Aug. 1993, pp. 262–281.
7. Dong, Z., Fundamental Problems in Computational Acoustics. Ph.D. Thesis, 1994, Florida State University.
8. Tam, C.K.W., "Advances in Numerical Boundary Conditions for Computational Aeroacoustics." AIAA Paper 97-1774, June 1997 (to appear in the Journal of Computational Acoustics).
9. Tam, C.K.W. and Dong, Z., "Radiation and Outflow Boundary Conditions for Direct Computation of Acoustic and Flow Disturbances in a Nonuniform Mean Flow," Journal of Computational Acoustics, Vol. 4, June 1996, pp. 175–201.
10. Tam, C.K.W. and Dong, Z., "Wall Boundary Conditions for High-Order Finite Difference Schemes in Computational Aeroacoustics," Theoretical and Computational Fluid Dynamics, Vol. 8, 1994, pp. 303–322.
11. Tam, C.K.W., Webb, J.C., and Dong, Z., "A Study of the Short Wave Components in Computational Acoustics," Journal of Computational Acoustics, Vol. 1, Mar. 1993, pp. 1–30.
12. Tam, C.K.W. and Shen, H., "Direct Computation of Nonlinear Acoustic Pulses Using High-Order Finite Difference Schemes," AIAA Paper 93-4325, Oct. 1993.
13. Westley, R. and Woolley, J.H., "An Investigation of the Near Noise Fields of a Choked Axisymmetric Air Jet," Proceedings of AFOSR-UTIAS Symposium on Aerodynamic Noise, Toronto, May 1968, pp. 147–167.
14. Norum, T.D., "Screech Suppression in Supersonic Jets," AIAA Journal, Vol. 21, Feb. 1983, pp. 235–240.
15. Ponton, M.K. and Seiner, J.M., "The Effects of Nozzle Exit Lip Thickness on Plume Resonance," Journal of Sound and Vibration, Vol. 154, No. 3, 1992, pp. 531–549.
16. Lau, J.C., "Effects of Exit Mach Number and Temperatures on Mean-Flow and Turbulence Characteristics in Round Jets," Journal of Fluid Mechanics, Vol. 105, 1981, pp. 193–218.
17. Norum, T.D. and Brown, M.C, "Simulated High-Speed Flight Effects on Supersonic Jet Noise." AIAA Paper 93-4388, Oct. 1993.
18. Tam, C.K.W. and Burton, D.E., "Sound Generated by Instability Waves of Supersonic Flows. Part 1, Two Dimensional Mixing Layers; Part 2, Axisymmetric Jets," Journal of Fluid Mechanics, Vol. 135, 1984, pp. 249–295.
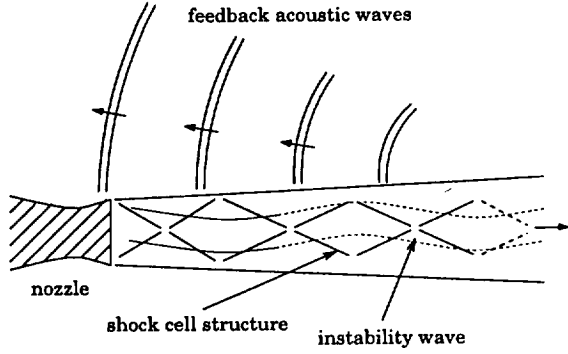
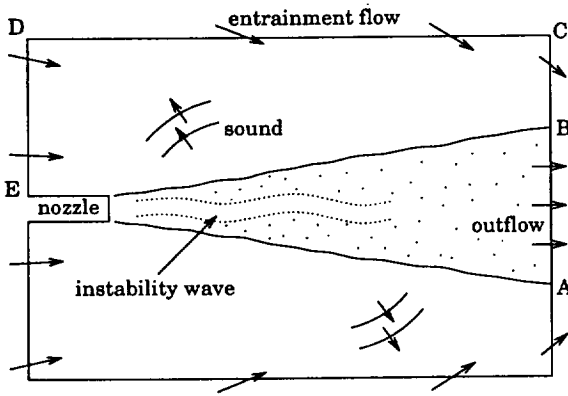Figure 1. Schematic diagram of the screech tone feedback loop.
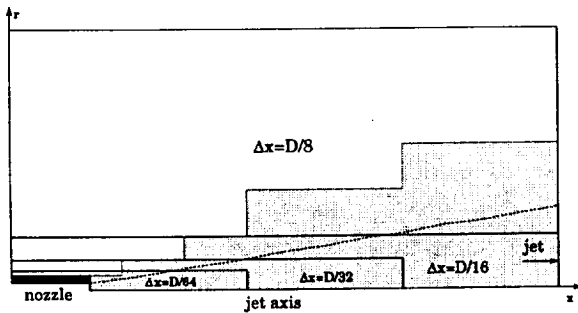

Figure 2. The physical domain to be simulated.

Figure 3. The computation domain in the $r - x$ plane showing the different subdomain and mesh sizes.
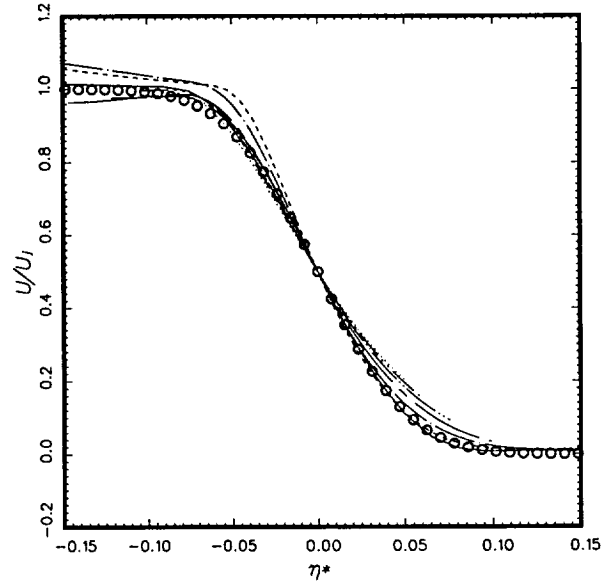

Figure 5. Comparison between mean velocity profiles of numerical simulation at $M_j = 1.2$. ———, $x/D = 1.0$, - - - -, $x/D = 2.0$, —·—, $x/D = 3.0$, —·—, $x/D = 4.0$, —··—, $x/D = 5.0$, —··—, $x/D = 6.0$, ······ , $x/D = 7.0$, and $U/U_j = 0.5[1 - erf(\sigma\eta^*)]$, O , $\sigma = 17$ from experiment (Lau 1981).
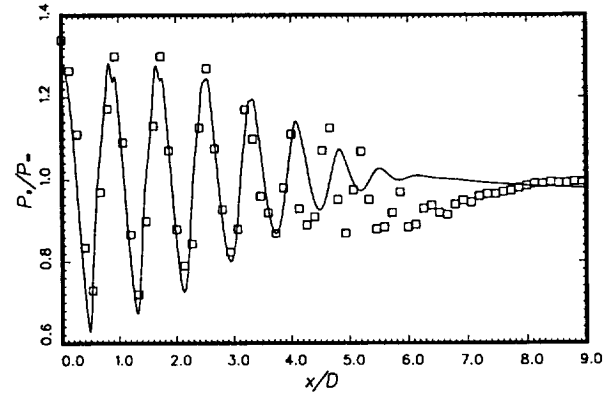
Figure 6. Comparison between calculated time-averaged pressure distribution along the centerline of a Mach 1.2 cold jet and the measurement of Norum and Brown (1993). ——— simulation, □ experiment.
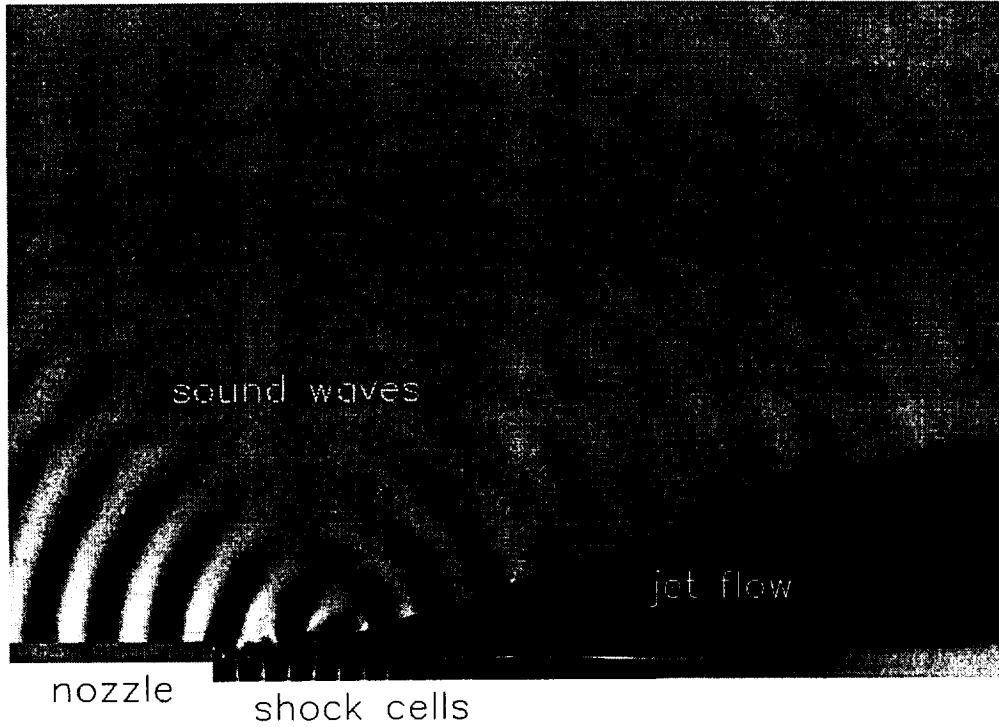
8

Figure 4. Density field from numerical simulation showing the generation and radiation of screech tone associated with a Mach 1.13, cold supersonic jet from a convergent nozzle.
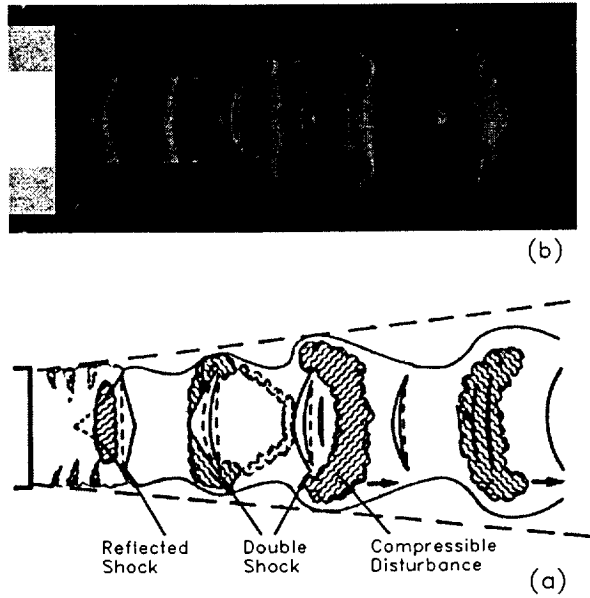
Figure 7. Unsteady shock cell structure and large scale disturbances inside the jet plume at an instant. (a) Experimental observation by Westley and Woolley (1968). (b) Numerical simulation.

Figure 9. Intensity of axisymmetric screech tones at the nozzle exit plane. (a) $r/D = 0.889$, (b) $r/D = 0.642$. Experiment (Ponton and Seiner, 1992): O A_1 mode, □ A_2 mode. Numerical simulation: ● A_1 mode, ■ A_2 mode.
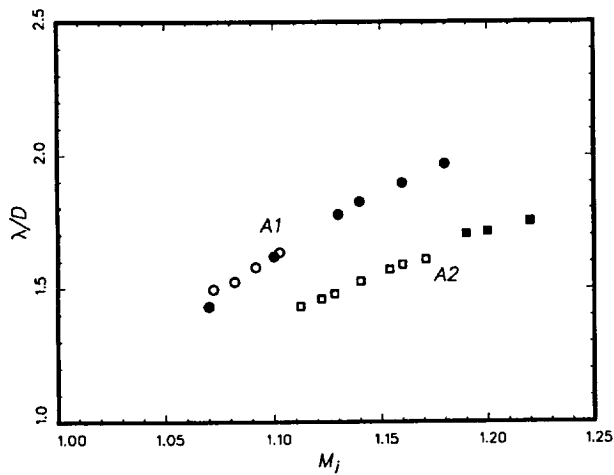

Figure 8. Comparison between the acoustic wavelengths of simulated screech tones and the measurements of Ponton and Seiner (1992). O, □ Measurements; ●, ■ simulation.
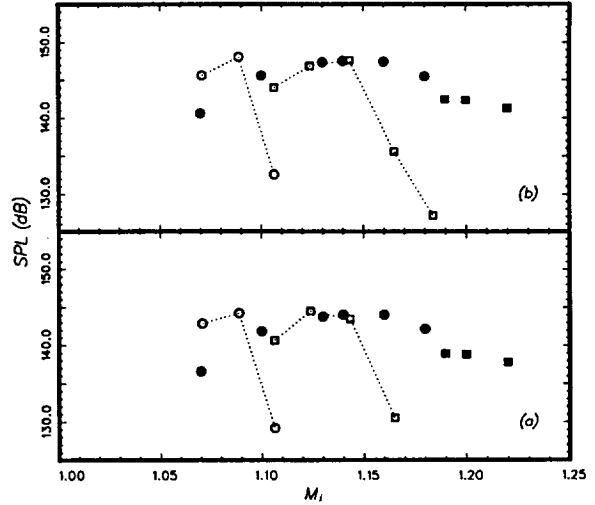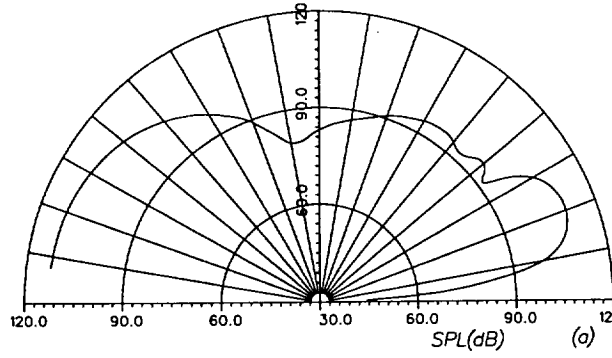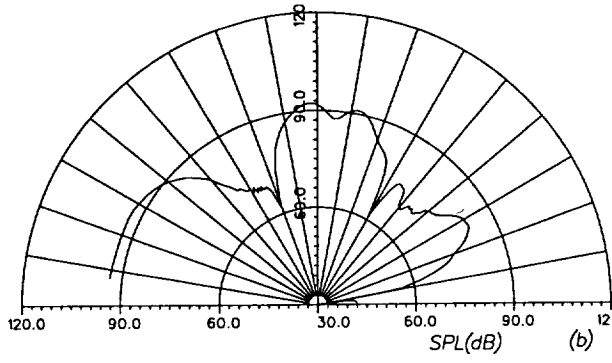
10

Figure 10. Directivity of the A_1 mode screech tone at $M_j = 1.18$, $r = 65D$. (a) Fundamental frequency, (b) second harmonic.
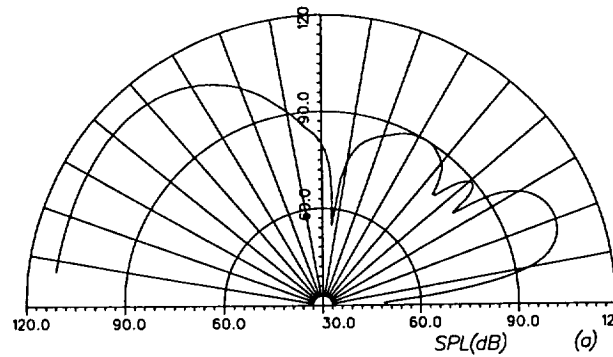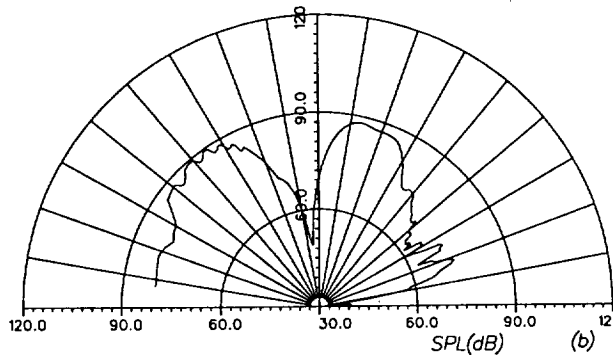

Figure 11. Directivity of the A_2 mode screech tone at $M_j = 1.2$, $r = 65D$. (a) Fundamental frequency, (b) second harmonic.

11

Advances in Numerical Boundary Conditions for Computational Aeroacoustics[†]

Christopher K.W. Tam[*]
Florida State University
Tallahassee, FL 32306-3027

Abstract

Advances in Computational Aeroacoustics (CAA) depend critically on the availability of accurate, nondispersive, least dissipative computation algorithm as well as high quality numerical boundary treatments. This paper focuses on the recent developments of numerical boundary conditions. In a typical CAA problem, one often encounters two types of boundaries. Because a finite computation domain is used, there are external boundaries. On the external boundaries, boundary conditions simulating the solution outside the computation domain are to be imposed. Inside the computation domain, there may be internal boundaries. On these internal boundaries, boundary conditions simulating the presence of an object or surface with specific acoustic characteristics are to be applied. Numerical boundary conditions, both external or internal, developed for simple model problems are reviewed and examined. Numerical boundary conditions for real aeroacoustic problems are also discussed through specific examples. The paper concludes with a description of some much needed research in numerical boundary conditions for CAA.

1. Introduction

A physical problem is defined mathematically by the governing equations and boundary conditions. When the governing equations are discretized to be solved computationally, the resulting finite difference equations are usually of higher order than the original partial differential equations. This is because high order schemes are needed to minimize numerical dispersion, an important requirement of Computational Aeroacoustics (CAA). The use of high order schemes will be assumed throughout this paper. High order finite difference equations support extraneous solutions that are not solutions of the partial differential equations. Thus to ensure a quality solution, a set of numerical boundary conditions must be specified such that not only the physical boundary conditions are faithfully reproduced but also the amplitude of the extraneous solutions, if generated, would be minimized.

A computation domain is inevitably finite in size. The result is that part of the physical domain is lost in the numerical simulation. It is, therefore, important that whatever takes place in the lost domain should have very little influence on the solution inside the computation domain. If this is not the case, the effects must be simulated by the boundary conditions imposed on the boundaries of the computation domain. For exterior aeroacoustics problems, a set of nonreflecting or outflow boundary conditions are needed at the external boundaries. The purpose of the nonreflecting or outflow boundary conditions is to allow the radiated sound waves and the convected vorticity and entropy waves to leave the computation domain smoothly without reflection.

The main objective of this paper is to provide an assessment of the recent advances in the formulation of numerical boundary conditions for aeroacoustics problems. In CAA, numerical boundary conditions are often developed for idealized model problems. In practical applications, they must be modified or extended to account for the presence of a nonuniform and sometimes unknown mean flow. In many cases, the outgoing wave amplitude is not necessarily small. So linear boundary conditions would need to be adjusted to allow the exit of nonlinear waves. Issues of this kind will also be examinined and discussed in this paper.

Broadly speaking, CAA boundary conditions can be classified into six categories. They are:

1. Radiation boundary conditions.
2. Outflow boundary conditions.
3. Wall boundary conditions.
4. Impedance boundary conditions.
5. Radiation/outflow boundary conditions with incoming acoustics or vorticity waves.
6. Radiation boundary conditions for ducted environments.

The first three categories of boundary conditions are also needed in standard Computational Fluid Dynamics (CFD). However, owing to the presence of acoustic and vorticity waves, the actual boundary conditions used in CAA are very different from those

[*] Distinguished Research Professor, Department of Mathematics. Associate Fellow AIAA.

used in traditional CFD. The last three categories of boundary conditions appear to be unique to CAA problems.

The need for the above types of boundary conditions is best illustrated by considering the two computational aeroacoustics problems shown in figures 1 and 2. Figure 1 shows the computation domain for numerical simulation of jet noise generation. The jet flow leaves the computation domain along boundary AB. Here the imposition of a set of outflow boundary conditions to allow the jet flow, sound, vorticity and entropy waves to exit smoothly would be most appropriate. Along boundary $BCDE$, radiation boundary conditions are required. Along the nozzle wall, wall boundary conditions are necessary. Figure 2 shows the computation domain for numerical simulation of fan noise radiation from a jet engine inlet. An important component of fan noise is generated by the interaction of the ingested vorticity waves and the rotor inside the engine. To suppress fan noise, a standard practice is to install sound absorbing liners on the inner surface of the engine inlet as shown in figure 2. These liners are represented mathematically by an impedance boundary condition. Along the exterior boundary $CDEF$, radiation boundary conditions with incoming vorticity waves are needed for the numerical simulation. Along internal boundary AB, radiation boundary conditions for ducted environment are required to simulate the internal propagation of acoustic duct modes inside the jet engine.

The rest of this paper is as follows. In Section 2, numerical boundary conditions developed using idealized flow models will be examined and compared. In Section 3, boundary conditions developed for more realistic aeroacoustics problems are presented. These two sections form the main part of this paper. Section 4 concludes with a discussion of the challenges and future directions of development in numerical boundary conditions for CAA.

2. Boundary Conditions Based on Idealized Model Problems

Most numerical boundary conditions available in the literature were developed for idealized model problems. Idealization, in some cases, are necessary to make it possible for a rigorous derivation of the boundary conditions. From the point of view that boundary conditions are local relations, the use of local approximations to formulate first-order boundary conditions is quite justified. The development of numerical boundary conditions for the acoustic wave equation has continued for many years. A recent review was given by Givoli[1]. For numerical boundary conditions relevant to CAA for which the Euler or Navier-Stokes equations are used, brief reviews can be found in the articles by Tam[2] and Lele[3].

2.1 Radiation/Inflow and Outflow Boundary Conditions

It is well known that in a uniform mean flow the linearized Euler equations support three types of disturbances. They are the acoustic waves, the vorticity waves and the entropy waves. The acoustic waves propagate at sound speed relative to the mean flow. The vorticity as well as the entropy waves are frozen patterns convected downstream by the mean flow. Because of the presence of the three types of wave disturbances, each having distinct propagation characteristics, the outgoing disturbances present at the inflow and outflow boundaries are very different. At an inflow boundary, the only outgoing disturbances are acoustic waves. At an outflow boundary, in addition to the acoustic waves, both vorticity and entropy waves are convected out by the mean flow. Due to this distinctive difference, some authors choose to separate radiation/inflow boundary conditions and outflow boundary conditions as two different types of boundary conditions. Here we will do so whenever clarity demands.

There have been many proposed radiation/inflow and outflow boundary conditions based on totally different considerations. For convenience, we will group them into five types as follows.

(a) Characteristics Based Boundary Conditions

Thompson[4,5] and Poinsat & Lele[6] proposed to treat the problem as one-dimensional near the boundary of the computation domain. The coordinate in the direction normal to the boundary is taken as the spatial coordinate. For Euler equations in one dimension, a full set of characteristics can be easily found. Thompson, Poinsat & Lele used these characteristics to form boundary conditions involving only outgoing waves. However, in two- or three-dimensional problems, there are no true characteristics. The characteristics boundary conditions work well for acoustic disturbances incident nearly normally on the boundary. They do not give good results at grazing angle of incidence or when there is a strong mean flow tangential to the boundary.

(b) Boundary Conditions Derived from Asymptotic Solutions

Bayliss & Turkel[7,8], Hagstrom & Hariharan[9]

and Tam & Webb[10] derived radiation and outflow boundary conditions by means of the asymptotic solutions of the governing equations. In the case of small amplitude disturbances superimposed on a uniform mean flow of density ρ_0, pressure p_0 and velocity u_0 in the x-direction, the linearized Euler equations in two dimensions are,

$$\frac{\partial \mathbf{U}}{\partial t} + \frac{\partial \mathbf{E}}{\partial x} + \frac{\partial \mathbf{F}}{\partial y} = \mathbf{H} \qquad (1)$$

where

$$\mathbf{U} = \begin{bmatrix} \rho \\ u \\ v \\ p \end{bmatrix}, \quad \mathbf{E} = \begin{bmatrix} \rho_0 u + \rho u_0 \\ u_0 u + \frac{p}{\rho_0} \\ u_0 v \\ u_0 p + \gamma p_0 u \end{bmatrix}, \quad \mathbf{F} = \begin{bmatrix} \rho_0 v \\ 0 \\ \frac{p}{\rho_0} \\ \gamma p_0 v \end{bmatrix}.$$

The nonhomogeneous term $\mathbf{H}$ on the right side of (1) represents distributed unsteady sources. By using Fourier-Laplace transforms, Tam & Webb[10] showed that the initial value problem of (1) has asymptotic solutions consisting of acoustic, vorticity and entropy waves. These asymptotic solutions have the form

(i) Acoustic waves

$$\begin{bmatrix} \rho \\ u \\ v \\ p \end{bmatrix} \sim \frac{F(\frac{r}{V(\theta)} - t, \theta)}{r^{\frac{1}{2}}} \begin{bmatrix} \frac{1}{a_0^2} \\ \hat{u}(\theta) \\ \hat{v}(\theta) \\ 1 \end{bmatrix} + O\left(r^{-\frac{3}{2}}\right) \qquad (2)$$

where (r, θ) are the polar coordinates. $V(\theta) = u_0 \cos\theta + a_0(1 - M^2 \sin^2\theta)^{\frac{1}{2}}$, $M = \frac{u_0}{a_0}$, $a_0 = \left(\frac{\gamma p_0}{\rho_0}\right)^{\frac{1}{2}}$ is the speed of sound.

(ii) Vorticity waves

$\rho = p = 0$

$$\begin{bmatrix} u \\ v \end{bmatrix} = \begin{bmatrix} \frac{\partial \Psi}{\partial y} \\ -\frac{\partial \Psi}{\partial y} \end{bmatrix} \qquad (3)$$

where

$$\Psi = \begin{cases} \Psi(x - u_0 t, y), & x \to +\infty \\ 0, & x \to -\infty \end{cases}$$

(iii) Entropy waves

$u = v = p = 0$

$$\rho = \begin{cases} \chi(x - u_0 t, y), & x \to +\infty \\ 0, & x \to -\infty \end{cases} \qquad (4)$$

In (2) to (4), the functions F, Ψ and χ depend on the initial condition and the unsteady source distribution.

At boundaries where there are only outgoing acoustic waves, a set of radiation boundary conditions can be derived by eliminating the unknown function F from (2) by first taking the t (time) and r derivatives. The resulting radiation boundary conditions are,

$$\left(\frac{1}{V(\theta)}\frac{\partial}{\partial t} + \frac{\partial}{\partial r} + \frac{1}{2r}\right) \begin{bmatrix} \rho \\ u \\ v \\ p \end{bmatrix} = 0 + O\left(r^{-\frac{5}{2}}\right). \qquad (5)$$

At the outflow region, the outgoing disturbances consist of a combination of acoustic, vorticity and entropy waves, that is, a direct sum of (2), (3) and (4). It turns out, it is possible to eliminate the unknown functions F, Ψ and χ, and upon using the linearized momentum equations of (1), to obtain the following set of outflow boundary conditions.

$$\frac{\partial \rho}{\partial t} + u_0 \frac{\partial \rho}{\partial x} = \frac{1}{a_0^2}\left(\frac{\partial p}{\partial t} + u_o \frac{\partial p}{\partial x}\right)$$

$$\frac{\partial u}{\partial t} + u_0 \frac{\partial u}{\partial x} = -\frac{1}{\rho_0}\frac{\partial p}{\partial x}$$

$$\frac{\partial v}{\partial t} + u_o \frac{\partial v}{\partial x} = -\frac{1}{\rho_0}\frac{\partial p}{\partial y} \qquad (6)$$

$$\frac{1}{V(\theta)}\frac{\partial p}{\partial t} + \cos\theta \frac{\partial p}{\partial x} + \sin\theta \frac{\partial p}{\partial y} + \frac{p}{2r} = 0.$$

Extensive numerical experiments testing the accuracy of (5) and (6) have been carried out. The results indicate that radiation boundary conditions (5) and outflow boundary conditions (6) are extremely effective, provided the sources are sufficiently far from the boundary of the computation domain. When there are sources located close to the boundary, the quality of the numerical solution is somewhat degraded.

(c) Absorbing Boundary Conditions

A different idea to deal with exterior boundary conditions is to use an absorbing layer. An absorbing layer usually consists of 10 to 20 mesh points in which damping terms are introduced to damp out the incident waves. The development of absorbing boundary conditions has been pursued by many investigators including Engquist & Majda[11], Higdon[12,13], Kosloff & Kosloff[14] and Jiang & Wong[15].

In a more recent work, the idea of absorbing the incident wave was extended and refined by Colonius *et*

3

al. into a sponge and exit zone with grid stretching and filtering. Their work is directly related to the earlier work by Rai & Moin[17]. Similar proposal but without grid stretching was advanced before by Israeli and Orszag[18]. A somewhat different approach was suggested by Ta'asan & Nark[19]. They artificially modified the governing equations in a buffer zone so that the mean flow becomes supersonic in the outward direction. This idea was further extended by Hayden and Turkel[20] to the full Euler equations in conservation form. Most recently Freund[21] proposed a zonal approach combining the absorbing boundary idea and the technique of Ta'asan & Nark.

(d) Perfectly Matched Layer

In an absorbing layer, the addition of artificial damping terms to the governing equations for the purpose of damping out the incidence disturbances also can lead to substantial reflections at the interface. Berenger[22,23], in his work on computational electromagnetics, found that it is possible to formulate an absorbing layer without reflection. Such a layer has come to be known as a perfectly matched layer (PML). It has found applications in computational aeroacoustics, elastic wave propagation[24] and other areas. Hu[25] was the first to apply PML to acoustics problems governed by the linearized Euler equations with uniform mean flow. He has since extended his work to nonuniform flow and for the fully nonlinear Euler equations[26]. Further applications of PML can be found in the recent works of Hu and coworkers[27,28]. One great advantage of the PML method is that if the mean flow is uniform the boundary of the computation domain can be put very close to the acoustic sources. This sometimes allows the use of a small computation domain.

Although PML has been demonstrated to perform exceedingly well computationally yet the PML equations with a mean flow are unstable. Consider the computation of small amplitude disturbances superimposed on a uniform mean flow in a computation domain as shown in figure 3. Let's use $\Delta x = \Delta y$ (the mesh size) as the length scale, a_0 (the sound speed) as the velocity scale, $\frac{\Delta x}{a_0}$ as the time scale, $\rho_0 a_0^2$ (where ρ_0 is the mean density) as the pressure scale. The dimensionless governing equations in the PML are formed by splitting the linearized Euler equations according to the spatial derivatives. An absorption term is added to each of the equations with spatial derivative in the direction normal to the layer. For example, for the PML on the right boundary of figure 3, region (1), the governing equations

are[25],

$$\frac{\partial u_1}{\partial t} + \sigma u_1 + M_x \frac{\partial}{\partial x}(u_1 + u_2) + \frac{\partial}{\partial x}(p_1 + p_2) = 0$$

$$\frac{\partial u_2}{\partial t} + M_y \frac{\partial}{\partial y}(u_1 + u_2) = 0$$

$$\frac{\partial v_1}{\partial t} + \sigma v_1 + M_x \frac{\partial}{\partial x}(v_1 + v_2) = 0 \qquad (7)$$

$$\frac{\partial v_2}{\partial t} + M_y \frac{\partial}{\partial y}(v_1 + v_2) + \frac{\partial}{\partial y}(p_1 + p_2) = 0$$

$$\frac{\partial p_1}{\partial t} + \sigma p_1 + M_x \frac{\partial}{\partial x}(p_1 + p_2) + \frac{\partial}{\partial x}(u_1 + u_2) = 0$$

$$\frac{\partial p_2}{\partial t} + M_y \frac{\partial}{\partial y}(p_1 + p_2) + \frac{\partial}{\partial y}(v_1 + v_2) = 0$$

where M_x and M_y are the mean flow Mach numbers in the x and y directions. σ is the absorption coefficients.

Suppose we look for solutions with (x, y, t) dependence in the form $\exp[i(\alpha x + \beta y - \omega t)]$. It is easy to find from (7) that the dispersion relations of the PML region are,

$$\left(1 - \frac{\alpha M_x}{\omega + i\sigma} - \frac{\beta M_y}{\omega}\right)^2 - \frac{\alpha^2}{(\omega + i\sigma)^2} - \frac{\beta^2}{\omega^2} = 0 \quad (8)$$

$$1 - \frac{\alpha M_x}{\omega + i\sigma} - \frac{\beta M_y}{\omega} = 0 \qquad (9)$$

In the limit $\sigma \to 0$, (8) and (9) become the dispersion relations of the acoustic and the vorticity waves of the linearized Euler equations. (8) is a quadric equation in ω. It has two extra roots in addition to the two modified acoustic modes. For small σ, the two spurious roots are damped but one of the modified acoustic roots is unstable. For larger σ, numerical solutions indicate that one of the spurious roots becomes unstable. In any case, the equation splitting procedure and the addition of an absorption term, both are vital to the suppression of reflections at the interface between the computation domain and the PML, inadvertently lead to instabilities.

For small σ, the roots of (8) and (9) can be found by perturbation. Let,

$$\omega^{(a)} = \omega_0^{(a)} + \sigma \omega_1^{(a)} + \sigma^2 \omega_2^{(a)} + \dots \qquad (10)$$

$$\omega^{(v)} = \omega_0^{(v)} + \sigma \omega_1^{(v)} + \sigma^2 \omega_2^{(v)} + \dots \qquad (11)$$

where the roots of (8) and (9) are designated by a superscript 'a' (for acoustic waves) and 'v' (for

4

vorticity waves). Substitution of (10) and (11) into (8) and (9), it is straightforward to find,

$$\omega_0^{(a)} = \omega_+, \quad \omega_-, \quad 0, \quad 0 \qquad (12)$$

where

$$\omega_\pm = (\alpha M_x + \beta M_y) \pm (\alpha^2 + \beta^2)^{\frac{1}{2}}$$

$$\omega_1^{(a)} = i \left[\frac{-\omega_\pm^2 + (\alpha M_x + \beta M_y)\omega_\pm + (1 - M^2)\beta^2 - \alpha\beta M_x M_y}{\omega_\pm(\omega_\pm - \alpha M_x - \beta M_y)} \right] \qquad (13)$$

$$\omega_0^{(v)} = \alpha M_x + \beta M_y, \quad 0 \qquad (14)$$

$$\omega_1^{(v)} = \frac{-i}{1 + (\frac{M_y}{M_x})(\frac{\beta}{\alpha})} \qquad (15)$$

Clearly if $\omega_1^{(a)}$ or $\omega_1^{(v)}$ has positive imaginary part, the mode is unstable. (13) has a simple interpretation in the case $M_y = 0$. In this special case, (13) reduces to

$$\omega_1^{(a)} = i \left[\frac{\alpha^2 M_x^2 - \alpha\omega_\pm M_x}{\beta^2 + \alpha\omega_\pm M_x - \alpha^2 M_x^2} \right]. \qquad (16)$$

For acoustic waves with negative phase velocity; i.e., $\alpha\omega_\pm < 0$ (the group velocity can, however, be positive) the numerator of (16) is positive, there will be values of β^2 for which $\omega_1^{(a)}$ is purely positive imaginary. Similarly, from (15), for $\frac{\beta}{\alpha} < 0$ and $|\frac{\beta}{\alpha}| > \frac{M_x}{M_y}$, $\omega_1^{(v)}$ is also purely positive imaginary. Thus the PML equations in the presence of a uniform flow with $M_x \neq 0$ support unstable solutions.

In a finite difference computation the dimensionless wavenumbers α and β are restricted to the range of $-\pi$ to π. Following the work of Hu[25], we will assume a PML of width equal to 10 mesh spacings. For a mean flow of $M_x = 0.3$, a value of $\sigma = 1.5$ would be quite sufficient to reduce the intensity of the incident acoustic waves by a factor of 10^5. Figure 4 shows a contour map of the growth rate of the most unstable wave (Im(ω) is largest) in the $\alpha - \beta$ plane for such a mean flow. The maximum growth rate is 0.035. In carrying out numerical simulation over a long period of time, even a weak instability could be a source of trouble. It is, therefore, desirable to suppress the instability. One way to suppress the instability and, at the same time, retain perfectly matched condition at the edge of the computation domain is to add artificial selective damping

terms[29] to the discretized form of (7). The design of the artificial selective damping stencil is such that there is almost no damping on the long (physical) waves. Thus the inclusion of these terms in the finite difference scheme should not alter the perfectly matched condition for the physical waves. With artificial damping included, the discretized form of the first equation of (7) according to the 7-point stencil Dispersion-Relation-Preserving (DRP) scheme[10] is (Note: all the other equations are to be treated in a similar way),

$$K_{\ell,m}^{(n)} = -\sigma u_{1\ell,m}^{(n)} - M_x \sum_{j=-3}^{3} a_j [u_{1\ell+j,m}^{(n)} + u_{2\ell+j,m}^{(n)} + p_{1\ell+j,m}^{(n)} + p_{2\ell+j,m}^{(n)}]$$

$$- \frac{1}{R_\Delta} \left[\sum_{j=-3}^{3} d_j \left(u_{1\ell+j,m}^{(n)} + u_{1\ell,m+j}^{(n)} \right) \right] (17)$$

$$u_{1\ell,m}^{(n+1)} = u_{1\ell,m}^{(n)} + \Delta t \sum_{j=0}^{3} b_j K_{\ell,m}^{(n-j)} \qquad (18)$$

where R_Δ is the artificial mesh Reynolds numbers. By applying Fourier transform analysis to (17) and (18) following Ref. [29], the damping rate introduced by the last term of (17) is

$$D(\alpha, \beta) = \frac{1}{R_\Delta} \sum_{j=-3}^{3} d_j \left(e^{-ij\alpha} + e^{-ij\beta} \right) \qquad (19)$$

Figure 5 shows the contours of constant damping rate for $R_\Delta = 1.0$. The coefficient d_j's are those corresponding to $\sigma = 0.3\pi$ given in the appendix of Ref. [2]. Figure 6 shows the combined growth and damping rate of figures 4 and 5 for $R_\Delta = 0.46$. As can be seen, the instability is completely suppressed. Note that for a PML with a width of 10 mesh spacings, waves with a wavenumber α smaller than $\frac{2\pi}{10}$ cannot be excited. This band of wavenumbers lies within the two vertical dotted lines of figure 6.

(e) Other Methods

In addition to the above four types of methods, nonreflecting boundary conditions have also been developed by a number of investigators using special methodology. This includes the works of Giles[30], Atkins & Casper[31], Colonius[32], Scott et al.[33], Kroner[34] and Roe[35]. Giles used a Fourier series approach. His work appears to have been motivated by turbomachinery noise and flow consideration.

5

(f) Evaluation of Radiation/Inflow and Outflow Boundary Conditions

During the last few years, there have been a number of papers reporting the results of evaluations of the performance and accuracy of a number of proposed radiation and outflow boundary conditions. Hixson et al.[36] employed a CAA problem with known exact solution to evaluate the quasi-one-dimensional characteristic boundary conditions of Thompson[4,5], the Fourier series boundary conditions of Giles and the asymptotic boundary conditions of Tam & Webb[10] and Bayliss & Turkel[7,8]. They reported that the Tam & Webb boundary conditions gave satisfactory results whereas the Thompson's boundary conditions produced significant reflections.

Hayden & Turkel[37] reported their experience in using the boundary condition of a number of investigators[4,5,7,8,9,10,33,34,35]. However, the various proposed boundary conditions were not implemented in the computation in an identical manner. A definitive comparison becomes impossible. Dong[38], in a study of radiation boundary conditions for nonuniform mean flow, performed a direct comparison of the results using his method and those of the Thompson's and Tam & Webb's boundary conditions. The numerical results confirm the finding of Hixson et al.[36], namely, the quasi-one-dimensional characteristics boundary conditions can cause significant reflections and inaccuracies.

It is also worthwhile to mention that two CAA workshops on benchmark problems have been held since 1994. Some of the benchmark problems were designed to test radiation/inflow and outflow boundary conditions. In each of the workshop proceedings[39,40], there is a section on comparisons of computed results and exact (nearly exact) solutions. They provide a measure of the quality of the various numerical boundary conditions used.

2.2 Wall Boundary Conditions for High-Order Schemes

In CAA, high order finite difference schemes are used because they have less numerical dispersion. However, a high order finite difference equation support spurious solutions that have no relationship to the original partial differential equation. These spurious solutions are unavoidably excited at a wall. For aeroacoustics problems, the spurious waves are of two types, propagating waves with short wave lengths and spatially damped waves. Thus when an acoustic wave pulse impinges on a wall, in addition to the reflected waves, spurious short waves

will also be emitted in a high order finite difference solution. Furthermore, the spatially damped waves would also be generated. But they decay as they propagate away from the wall. Effectively they form a numerical boundary layer on the wall surface.

There are two major difficulties in developing wall boundary conditions for high order finite difference schemes. First, high order finite difference equations require additional boundary conditions, beyond the physical boundary conditions of the original problem, to define a unique solution. These additional boundary conditions, or the way to handle the need for these boundary conditions, must be found so that only very small amplitude spurious waves are excited. Second, in the discretized system, each flow variable at either an interior or boundary mesh point is governed by an algebraic equation (discretized form of the partial differential equation). The number of unknowns is exactly equal to the number of equations. Thus there will be too many equations and not enough unknowns if it is insisted that the boundary conditions at the wall mesh point are satisfied also. This is, perhaps, one of the major differences between partial differential equations and finite difference equations.

In the literature, there is an absence of suggestions as how to impose wall boundary condition for high order schemes except for the work of Tam & Dong[41]. They proposed to use backward difference stencils as a wall is approached. This eliminates the need for extra boundary conditions. To provide enough unknowns to enforce the physical wall boundary conditions as well as to allow the discretized governing equations to be satisfied at mesh points on the wall, they suggested including ghost values at ghost points. Ghost points are mesh points immediately outside the computation domain. The number of ghost values to be included is equal to the number of physical wall boundary conditions per enforcement point. Tam & Dong carried out an analysis of the problem of reflection of plane acoustic waves by a plane wall using the ghost point method. They found that the intensity of the reflected spurious short waves is largest for normal incidence but is less than 0.4% of the amplitude of the incident wave if a resolution of 10 mesh spacings per acoustic wavelength is used. The thickness of the numerical boundary layer (defined as the distance from the wall at which the spurious damped numerical wave solution drops to 0.1% of the magnitude of the incident wave) is a little over one mesh spacing. The ghost point method has since been extended by Kurbatskii & Tam[42] for applications to curved wall surfaces us-

ing Cartesian mesh. Numerical results obtained in a number of test cases agreed well with exact solutions.

For acoustic wave scattering problems, Chung & Morris[43] proposed an Impedance Mismatched Method (IMM). In this method, solid bodies are replaced by a new fluid medium with a large characteristic impedance, ρa. When the characteristic impedance of the new fluid medium is infinite, it can be shown that the incident waves are completely reflected. The advantage of the IMM method is that the entire computation domain including the scattering bodies can be regarded as a continuous fluid region making the programming exceedingly simple. However, unlike the ghost point method, the IMM cannot be used for viscous problems.

2.3 Impedance Boundary Condition

One of the most successful methods for suppressing fan noise radiating out the inlets of jet engines is to install acoustic liners inside the front part of the engine inlet as shown in figure 2. Mathematically, a liner is represented by an impedance boundary condition. The impedance, Z, is a complex quantity. If the time dependence is taken to be $e^{-i\omega t}$ then Z is related to the two real parameters of the liner R, the resistance, and X, the reactance, by

$$Z = R - iX.$$

Ref. [44] provides a good introduction and many references to the impedance of liners. In the past, impedance boundary condition was analyzed in the frequency domain. For time marching computation, an equivalent time-domain impedance boundary condition is required.

Presently, two entirely different approaches for developing time-domain impedance boundary condition are available. Both approaches have limitations. Ozyoruk & Long[45,46], following the works of Sullivan[47] and Penny[48] in computational electromagnetics, employed the z-transform method in implementing the impedance boundary conditions in the time-domain. This method provides more flexibility in fitting the frequency dependence of the resistance and reactance of the liner to experimental measurements. Tam & Auriault[49] used a differential formulation of time-domain impedance boundary condition. Both methods are constrained by spurious numerical instability. For treatment of broadband noise problems, the formulation of Tam & Auriault is restricted by numerical instability to a 3 parameter model. Further improvements on these methods are obviously desirable.

2.4 Radiation and Outflow Boundary Conditions with Incoming Acoustic and Vorticity Waves

As depicted in figure 2, there are aeroacoustics problems for which unsteady incoming acoustic or vorticity waves are an important part of the problem. For this class of problems, the boundary conditions must allow the incoming disturbances to propagate in and the outgoing disturbances to leave the computation domain smoothly. There are two ways to treat these boundary requirements. We will refer to them as the nonhomogeneous boundary conditions method and the split variable method.

The nonhomogeneous boundary conditions approach recognizes that the computed variables are the direct sum of the incoming and outgoing disturbances. Thus on using subscripts 'in' and 'out' to denote the part of the flow variables associated with the incoming and outgoing disturbances, the outgoing disturbances can be expressed as the difference between the computed variables and the prescribed incoming disturbances; e.g.,

$$\rho_{\text{out}} = \rho - \rho_{\text{in}}. \tag{20}$$

Now at the inflow boundary, the outgoing acoustic waves satisfy the radiation boundary condition (5). Therefore, by substitution of (20) and similar expressions into (5), a set of nonhomogeneous radiation boundary conditions is obtained,

$$\left[\frac{1}{V(\theta)} \frac{\partial}{\partial r} + \frac{\partial}{\partial t} + \frac{1}{2r} \right] \begin{bmatrix} \rho \\ u \\ v \\ p \end{bmatrix}$$

$$= \left[\frac{1}{V(\theta)} \frac{\partial}{\partial r} + \frac{\partial}{\partial t} + \frac{1}{2r} \right] \begin{bmatrix} \rho_{\text{in}} \\ u_{\text{in}} \\ v_{\text{in}} \\ p_{\text{in}} \end{bmatrix}. \tag{21}$$

In (21) the nonhomogeneous terms on the right side represent the known incoming waves. In Ref. [42], the plane acoustic wave scattering problem was calculated numerically using (21) as the boundary conditions. It has been found that if the computation is to be carried out with low spatial resolution, then an improvement in the numerical accuracy is obtained if the exact finite difference solution of the incoming disturbances is used on the right side of (21). At an outflow boundary, nonhomogeneous outflow boundary conditions similar to (21) may be derived from (6).

7

Another way to generate the incoming waves is to divide the computation domain into an interior and a boundary region. In the interior region, the computed variables are the sum of the outgoing and incoming disturbances. In the boundary region (3 mesh points for the 7-point DRP scheme), the governing equations are either the boundary conditions derived from asymptotic solutions of Section 2.1(b) or the absorbing boundary conditions of Section 2.1(c) or the PML equations of Section 2.1(d). The computed variables are the outgoing disturbances only. Whenever a derivative stencil extends to the other region, the value of the variable required can be obtained by using (20) and similar equations. Here the inflow variables are given so either ρ or ρ_{out}, whichever is appropriate can be easily found. In this way, the incoming disturbances are generated at the stencil overlapping part (overlapping with the boundary region) of the interior region.

2.5 Radiation Boundary Conditions for Ducted Environment

For the fan noise radiation problem illustrated in figure 2, when the sound waves, generated by the cutting of the ingested vorticity waves by the rotor, reach the opening of the jet engine inlet, part of them are reflected back. The reflected waves would be propagating in the form of duct modes if the internal area of the engine inlet varies slowly. Unlike acoustic waves in the free field, duct modes are dispersive. They are formed by the continuous reflection of sound waves by the walls of the duct. Their propagation characteristics are very different from acoustic waves in free space. As a result, not all the radiation and outflow boundary conditions discussed in Section 2.1 are applicable along boundary AB of figure 2.

In the Second CAA Workshop on Benchmark Problems[40], several benchmark problems require the use of radiation boundary conditions in a ducted environment for their solutions. For single frequency time periodic problems, Tam et al.[50] developed a set of such radiation boundary conditions using the duct modes as the basis. Hu and Manthey[28], on the other hand, used the PML and variable splitting method to form such radiation boundary conditions. It is necessary to point out that in a ducted environment, the dispersion relation of the PML equations are not the same as those given in (8) and (9). They are related to the duct modes. To ensure numerical stability, artificial selective damping is again required in the PML. The value of the artificial mesh Reynolds number, R_Δ, necessary to ensure stability

can be found in much the same way as in Section 2.1(d).

3. Boundary Conditions for Real Problems

The numerical boundary conditions discussed in the above section are based largely on simplified models. Real problems, however, are generally more complex. In many of these problems, numerical boundary conditions do not simply play a single role such as letting the outgoing disturbances exit smoothly with minimal reflections. They are to perform multiple tasks. In most problems that are of technological significance, the mean flow is nonuniform. Further, because of computer memory constraint and run time limitation, the size of the computation domain is usually smaller than ideal. The small computer domain, forcing the boundary to be closer to the source or objects in the flow, puts additional demand on the design of high quality numerical boundary conditions. There does not appear to have a systematic way of classifying numerical boundary conditions for real problems. We will illustrate, by specific examples, below how some of the model boundary conditions can be modified and extended for applications in practical CAA problems of current interest.

3.1 Radiation Boundary Conditions for Simulating Jet Noise Generation

Let us return to the computation domain for simulating jet noise generation in figure 1. For practical reasons, the size of the computation domain is typically 30 to 40 diameters in the axial direction and 20 to 30 diameters in the radial direction. These dimensions are smaller than those of the anechoic chambers in most physical experiments. Because of the proximity of the computation boundary to the jet flow, the boundary conditions along boundary $BCDE$ are burdened with multiple tasks. Obviously, the boundary conditions must be transparent to the outgoing acoustic waves radiated from the jet. In addition, the boundary conditions must impose the ambient conditions on the numerical solution. In other words, they specify the static conditions far away from the jet. Furthermore, the jet entrains a large volume of ambient fluid. The entrainment flow velocity at the computation boundary is although small yet not entirely negligible. For high quality numerical simulation, the boundary conditions must, therefore, allow the entrainment flow to enter the computation domain smoothly as well.

In a recent work, Tam & Dong[51] considered the need to formulate a set of radiation as well as out-

flow boundary conditions for situations where the mean flow was nonuniform. They provided a generalization of the asymptotic radiation boundary conditions (5) and outflow boundary conditions (6). Let $\bar{p}$, $\bar{u}$, $\bar{v}$ and $\bar{p}$ be the weakly nonuniform mean flow at the boundary of the computation domain, an appropriate set of radiation boundary conditions, in 3 dimensions, was found to be,

$$\frac{1}{V(\theta, r)} \frac{\partial}{\partial t} \begin{bmatrix} \rho \\ u \\ v \\ p \end{bmatrix}$$

$$+ \left[\sin\theta \frac{\partial}{\partial r} + \cos\theta \frac{\partial}{\partial x} + \frac{1}{(r^2 + x^2)^{\frac{1}{2}}} \right] \quad (22)$$

$$\begin{bmatrix} \rho - \bar{\rho} \\ u - \bar{u} \\ v - \bar{v} \\ p - \bar{p} \end{bmatrix} = 0$$

where (r, ϕ, x) are the cylindrical coordinates, θ is the polar angle (in spherical coordinates) with the x-axis as the polar axis. (u, v) are the velocity components in the axial (x) and radial (r) directions. $V(\theta, r) = \bar{u}\cos\theta + \bar{v}\sin\theta + [\bar{a}^2 - (\bar{v}\cos\theta - \bar{u}\sin\theta)^2]^{\frac{1}{2}}$ and $\bar{a}$ is the speed of sound.

In their work on numerical simulation of the generation of axisymmetric screech tones from imperfectly expanded supersonic jets (see Ref. [52] for a description of the jet screech phenomenon) Tam & Shen[53] considered a computation domain nearly identical to that of figure 1. They used (22) as the basis to develop the necessary radiation-entrainment flow numerical boundary conditions. It was recognized that the entrainment flow at the boundary of the computation domain would be influenced by the jet flow outside the computation domain. To develop an asymptotic entrainment flow solution Tam & Shen divided the jet into many evenly spaced segments as shown in figure 7. The jet extended beyond the computation domain to 60 diameters downstream. The mass fluxes across the boundaries of each segment was found using empirical jet flow data. The difference of the mass fluxes at the two ends of each segment of the jet gave the amount of entrainment flow for the particular segment. This entrainment was then simulated by a point source located at the center of the segment. The asymptotic solution for a point sink located on the x-axis at x_s in a compressible fluid is given by (a subscript 'e' is used to indicate entrainment flow),

$$\frac{\rho_e}{\rho_\infty} = 1 - \frac{Q^2}{32\pi^2[(x - x_s)^2 + r^2]^2} + \cdots$$

$$\frac{u_e}{a_\infty} = -\frac{Q(x - x_s)}{4\pi[(x - x_s)^2 + r^2]^{\frac{3}{2}}} + \cdots$$

$$\quad (23)$$

$$\frac{v_e}{a_\infty} = -\frac{Qr}{4\pi[(x - x_s)^2 + r^2]^{\frac{3}{2}}} + \cdots$$

$$\frac{p_e}{\rho_\infty a_\infty^2} = \frac{1}{\gamma} - \frac{Q^2}{32\pi^2[(x - x_s)^2 + r^2]^2} + \cdots$$

where ρ_∞, a_∞ and γ are the ambient gas density, sound speed and the ratio of specific heats. Q, the strength of the sink, has dimensions of $\rho_\infty a_\infty D^2$; D is the jet diameter. On replacing $(\bar{p}, \bar{u}, \bar{v}, \bar{p})$ of (22) by (ρ_e, u_e, v_e, p_e) of (23) and by summing over the contributions from all the sinks, the desired radiation entrainment flow boundary conditions are obtained.

Figure 8 shows the entrainment flow streamlines of a Mach 1.13 cold jet from a convergent nozzle obtained by numerical simulation. It is worthwhile to point out that along the right-hand boundary BC, the mean flow actually flows out of the computation domain, exactly as observed experimentally in the case of a free jet. This streamline pattern would be very different had the entrainment flow outside the computation domain not been included in the sink flow calculation. If a cut-off were imposed at the right boundary of the computation domain, a recirculation flow pattern would emerge. This, however, is inconsistent with experimental observation.

3.2 Outflow and Jet Axis Boundary Conditions for Simulating Jet Noise Generation

Jets are inherently unstable. The instability waves of jets play an important role in jet noise generation[52]. The instability waves, once excited at the nozzle lip region, grow rapidly as they propagate in the downstream direction. Since the jet spreads out in the downstream direction, it follows that the shear gradient and hence the instability growth rate decreases farther and farther downstream. Eventually the wave would reach a location downstream where it becomes damped. From this point on, the wave amplitude decreases continuously all the way to the outflow boundary. In the work of Tam & Shen[53] the outflow boundary was located at 30 jet diameters downstream. At this distance, the amplitudes of the decaying instability waves (sometimes

9

referred to as large turbulence structures when there is less coherence) are not small. To account for the weak nonlinearities of the outflow disturbances, it is possible to nonlinearize the outflow boundary conditions (6) by replacing the linearized terms by their nonlinear counterpart. This yields (in cylindrical coordinates),

$$\frac{\partial \rho}{\partial t} + u \frac{\partial \rho}{\partial x} = \frac{1}{a^2} \left(\frac{\partial p}{\partial t} + u \frac{\partial p}{\partial x} \right)$$

$$\frac{\partial u}{\partial t} + u \frac{\partial u}{\partial x} + v \frac{\partial u}{\partial r} = -\frac{1}{\rho} \frac{\partial p}{\partial x} \qquad (24)$$

$$\frac{\partial v}{\partial t} + u \frac{\partial v}{\partial x} + v \frac{\partial v}{\partial r} = -\frac{1}{\rho} \frac{\partial p}{\partial r}$$

$$\frac{1}{V(\theta)} \frac{\partial p}{\partial x} + \cos \theta \frac{\partial p}{\partial x} + \sin \theta \frac{\partial p}{\partial r} + \frac{p - \bar{p}}{(x^2 + r^2)^{\frac{1}{2}}} = 0$$

where $\bar{p}$ is the static pressure calculated by the entrainment flow model at the edge of the jet flow at the outflow boundary. In their jet screech tones simulation work, Tam & Shen[53] reported that (24) provided very satisfactory numerical results. No reflection of any significance had been detected.

In cylindrical coordinates, the governing equations have an apparent singularity at the jet axis ($r \to 0$). For instance, the continuity equation may be written in the form,

$$\frac{\partial \rho}{\partial t} + \frac{\partial \rho v}{\partial r} + \frac{\partial \rho u}{\partial x} + \frac{1}{r} \frac{\partial \rho w}{\partial \phi} + \frac{\rho v}{r} = 0. \qquad (25)$$

To handle the apparent singularity, a jet axis boundary condition may be derived by taking the formal limit of (25) as $r \to 0$. On noting that as $r \to 0$, $v \to 0$ while $w \to 0$ faster than r, the formal limit of (25) is,

$$\frac{\partial \rho}{\partial t} + 2 \frac{\partial \rho v}{\partial r} + \frac{\partial \rho u}{\partial x} = 0. \qquad (26)$$

(26), which has no apparent singularity at $r = 0$, is to be enforced at all the mesh points along the jet axis.

Experience indicates that the use of (26) at $r = 0$ inevitably leads to the generation of spurious short waves at the x-axis in a time marching simulation. The reason for this is simply that there is an abrupt change in the governing equations between the jet axis and the first row of mesh point off the axis. Such discontinuous change always leads to the radiation of short waves. For problems with axisymmetry, one may use the half-mesh displacement method[50] to avoid the discontinuity. The half mesh displacement method does not involve a change in governing

equations. It depends on the extension of the computation domain to the region $r < 0$ by symmetry and antisymmetry arguments.

3.3 Numerical Simulation of Airframe Noise Generation

During landing with the wing flaps of an aircraft down, the unsteady flow over the airframe is an important source of noise. In a series of experimental investigation, Kendall & Ahtye[54] identified a number of airframe noise sources; referred to as the flap side-edge noise, gap noise and trailing edge noise. One possible gap noise generation mechanism is unsteady flow separation around the gap between the wing and the flap. This possibility was investigated using a 2-D numerical simulation by Thies, Tam & Reddy[55]. For simplicity, both the wing and flap were approximated by flat plates as shown in figure 9. This figure, from the numerical simulation, shows large unsteady separation on the suction side of the flap. In performing the numerical simulation, a relatively small computation domain was used. At a speed of Mach 0.15 and an angle of attack of 6 degrees, there is a steady loading on the wing-flap combination. The steady loading produces a distortion on the mean flow that extends all the way to the boundary of the computation domain. To achieve a reasonably accurate simulation, the numerical boundary conditions must not only allow the unsteady disturbances to leave the computation domain but also account for the mean flow distortion. Unlike the model problems of section 2 or the work of Ref. [51], the difficulty here in formulating a set of radiation boundary conditions is that the mean flow is unknown *a priori*.

In order to take into consideration the change in the mean flow at the boundary of the computation domain due to the presence of the wing-flap combination, one can first determine the forms of the asymptotic solutions of both the mean flow and the unsteady disturbances. This can be done by solving the linearized Euler equations. On using the wing chord L as the length scale, u_∞ (incoming velocity) as the velocity scale, $\frac{L}{u_\infty}$ as the time scale, ρ_∞ (the ambient gas density) as density scale and $\rho_\infty u_\infty^2$ as the pressure scale, the dimensionless linearized Euler equations are,

$$\frac{\partial \rho}{\partial t} + \cos \alpha \frac{\partial \rho}{\partial x} + \sin \alpha \frac{\partial \rho}{\partial y} + \left(\frac{\partial u}{\partial x} + \frac{\partial v}{\partial y} \right) = 0$$

$$\frac{\partial u}{\partial t} + \cos \alpha \frac{\partial u}{\partial x} + \sin \alpha \frac{\partial u}{\partial y} = -\frac{\partial p}{\partial x} \qquad (27)$$

10

$$\frac{\partial v}{\partial t} + \cos\alpha\frac{\partial v}{\partial x} + \sin\alpha\frac{\partial v}{\partial y} = -\frac{\partial p}{\partial y}$$

$$\frac{\partial p}{\partial t} + \cos\alpha\frac{\partial p}{\partial x} + \sin\alpha\frac{\partial p}{\partial y} + \frac{1}{M^2}\left(\frac{\partial u}{\partial x} + \frac{\partial v}{\partial y}\right) = 0$$

where M is the Mach number and α is the angle of attack. The time independent solution of (27) can be found by introducing a velocity potential $\Phi(x,y)$ defined by

$$u = \frac{\partial\Phi}{\partial x}, \quad v = \frac{\partial\Phi}{\partial y}$$

$$\tag{28}$$

$$p = -\left(\cos\alpha\frac{\partial\Phi}{\partial x} + \sin\alpha\frac{\partial\Phi}{\partial y}\right), \quad \rho = M^2 p.$$

Substitution of (28) into (27) gives,

$$\left(\cos\alpha\frac{\partial}{\partial x} + \sin\alpha\frac{\partial}{\partial y}\right)\Phi$$

$$\tag{29}$$

$$-\frac{1}{M^2}\left(\frac{\partial^2\Phi}{\partial x^2} + \frac{\partial^2\Phi}{\partial y^2}\right) = 0.$$

(29) can be manipulated into the Laplace equation by introducing a rotation and dilation of coordinates. The general solution of the Laplace equation can be expressed in the form of a Fourier series in polar coordinates. The lowest order nontrivial solution for large r is in the form of a logarithmic function. When rewritten in the Cartesian coordinates, it is found,

$$\Phi(x,y) \rightarrow A\,\ell n\left[(x\cos\alpha + y\sin\alpha)^2\right.$$

$$\tag{30}$$

$$\left. + (1 - M^2)(x\sin\alpha - y\cos\alpha)^2\right]$$

where A is an unknown constant. In the gap noise problem, A represents the as yet unknown loading on the wing-flap combination.

It is straightforward to find by substituting (30) into (28), after some algebra, the following asymptotic results.

$$\left(\frac{\partial}{\partial r} + \frac{1}{r}\right)\begin{bmatrix}\rho\\u\\v\\p\end{bmatrix} = 0.$$

$$\tag{31}$$

Since only the leading term is kept in (30), (31) is valid to order r^{-2} for large r. On the other hand, the asymptotic radiation boundary conditions for acoustic waves in a uniform mean flow, from (5), is

$$\left(\frac{1}{V(\theta)}\frac{\partial}{\partial t} + \frac{\partial}{\partial r}\right)\begin{bmatrix}\rho\\u\\v\\p\end{bmatrix} = 0 + O\left(r^{-\frac{3}{2}}\right).$$

$$\tag{32}$$

A combined asymptotic boundary conditions in 2 dimensions that reduces to (32) for the time dependent component and (31) for the time independent component is,

$$\left(\frac{1}{V(\theta)}\frac{\partial}{\partial t} + \frac{\partial}{\partial r} + \frac{1}{r}\right)\begin{bmatrix}\rho\\u\\v\\p\end{bmatrix} = 0 + O\left(r^{-\frac{3}{2}}\right).$$

$$\tag{33}$$

On following the same reasoning, it is easy to derive a corresponding set of outflow boundary conditions suitable for use in a relatively small computation domain where weakly nonuniform two-dimensional mean flow is present. The equations are,

$$\frac{\partial\rho}{\partial t} + \cos\alpha\frac{\partial\rho}{\partial x} + \sin\alpha\frac{\partial\rho}{\partial y}$$

$$= M^2\left(\frac{\partial p}{\partial t} + \cos\alpha\frac{\partial p}{\partial x} + \sin\alpha\frac{\partial p}{\partial y}\right)$$

$$\frac{\partial u}{\partial t} + \cos\alpha\frac{\partial u}{\partial x} + \sin\alpha\frac{\partial u}{\partial y} = -\frac{\partial p}{\partial x}$$

$$\tag{34}$$

$$\frac{\partial v}{\partial t} + \cos\alpha\frac{\partial v}{\partial x} + \sin\alpha\frac{\partial v}{\partial y} = -\frac{\partial p}{\partial y}$$

$$\frac{1}{V(\theta)}\frac{\partial p}{\partial t} + \frac{\partial p}{\partial r} + \frac{p}{r} = 0.$$

Thies et al.[55] implemented (33) and (34) in their numerical simulations of gap noise and obtained very satisfactory results. Figure 10 shows the sound-pressure-level (SPL) contours in dB from the numerical simulation. The SPL contours below the wing form nearly concentric circles centered at the gap between the wing and the flap. This indicates that the source of noise originates from the gap region in agreement with the experimental observations of Kendall & Ahtye[54].

4. Concluding Remarks

During the last few years, a good deal of progress has been made in the development of numerical boundary conditions for CAA. Numerical examples have shown that many of these boundary conditions, when used in conjunction with high order finite difference schemes, are capable of providing high quality computational results. However, a closer scrutiny reveals that the predominant fraction of these recent works is devoted primarily to radiation and outflow boundary conditions. Other equally important types of boundary conditions such as wall boundary conditions, impedance boundary conditions do not appear to have received enough attention. The need for these other types of boundary conditions would definitely be greater in the future. For they are crucial to the application of CAA methods to fan noise, duct acoustics, propeller and turbomachinery noise problems.

In this paper, two very important items directly related to numerical boundary conditions have not been satisfactorily discussed. The first is the discretization and implementation of the numerical boundary conditions. Needless to say, the discretization process affects the accuracy and performance of a proposed boundary condition in a differential form. The implementation of the discretized boundary condition in relation to the time marching high order finite difference scheme used for the interior points would also have a significant impact on the overall accuracy and stability of the numerical solution. The second item is error estimate. From the point of view of designing a computational algorithm for the solution of a class of aeroacoustics problems, *a priori* estimate is essential. Here order of magnitude estimate is not very helpful. The real need is a quantitative error estimate. Most unfortunately, so far, very little work has been done. It is hoped that investigators interested in CAA would accept these two items as their immediate challenges.

Acknowledgment

References

1. Givoli, D., "Non-Reflecting Boundary Conditions," Journal of Computational Physics, Vol. 94, May 1991, pp. 1-29.
2. Tam, C.K.W., "Computational Aeroacoustics: Issues and Methods," AIAA Journal, Vol. 33, Oct. 1995, pp. 1788-1796.
3. Lele, S.K., "Computational Aeroacoustics: A Review," AIAA Paper 97-0018, Jan. 1997.
4. Thompson, K.W., "Time Dependent Boundary Conditions for Hyperbolic Systems," Journal of Computational Physics, Vol. 68, Jan. 1987, pp. 1-24.
5. Thompson, K.W., "Time Dependent Boundary Conditions for Hyperbolic Systems, II," Journal of Computational Physics, Aug. Vol. 89, 1990, pp. 439-461.
6. Poinsot, T.J. and Lele, S.K., "Boundary Conditions for Direct Simulations of Compressible Viscous Flows," Journal of Computational Physics, Vol. 101, July 1992, pp. 104-129.
7. Bayliss, A. and Turkel, E., "Radiation Boundary Conditions for Wavelike Equations," Communications on Pure and Applied Mathematics, Vol. 33, Nov. 1980, pp. 707-725.
8. Bayliss, A. and Turkel, E., "Far Field Boundary Conditions for Compressible Flows," Journal of Computational Physics, Vol. 48, Nov. 1982, pp. 182-199.
9. Hagstrom, T. and Hariharan, S.I., "Accurate Boundary Conditions for Exterior Problems in Gas Dynamics," Mathematics of Computation, Vol. 51, Oct. 1988, pp. 581-597.
10. Tam, C.K.W. and Webb, J.C., "Dispersion-Relation-Preserving Finite Difference Schemes for Computational Acoustics," Journal of Computational Physics, Vol. 107, Aug. 1993, pp. 262-281.
11. Engquist, B. and Majda, A., "Absorbing Boundary Conditions for the Numerical Simulation of Waves," Mathematics of Computation, Vol. 31, July 1977, pp. 629-651.
12. Higdon, R.L., "Absorbing Boundary Conditions for Difference Approximations to the Multi-Dimensional Wave Equation," Mathematics of Computation, Vol. 47, Oct. 1986, pp. 629-651.
13. Higdon, R.L., "Numerical Absorbing Boundary Conditions for the Wave Equation," Mathematics of Computation, Vol. 49, July 1987, pp. 65-90.
14. Kosloff, R. and Kosloff, D., "Absorbing Boundaries for Wave Propagation Problems," Journal of Computational Physics, Vol. 63, April 1986, pp. 363-376.
15. Jiang, H. and Wong, Y.S., "Absorbing Boundary Conditions for Second Order Hyperbolic Equations," Journal of Computational Physics, Vol 88., May 1990, pp. 205-231.
16. Colonius, T., Lele, S.K., and Moin, P., "Boundary Conditions for Direct Computation of Aero-

dynamic Sound Generation," AIAA Journal, Vol. 31, Sept. 1993, pp. 1574-1582.

17. Rai, M.M., and Moin, P., "Direct Numerical Simulation of Transition and Turbulence in a Spatially Evolving Boundary Layer," Journal of Computational Physics, Vol. 109, 1993, pp. 169-192.

18. Israeli, M., and Orszag, S.A., "Approximation of Radiation Boundary Condition," Journal of Computational Physics, Vol. 41, 1981, pp. 115-135.

19. Ta'asan, S., and Nark, D.M., "An Absorbing Buffer Zone Technique for Acoustic Wave Propagation," AIAA Paper 95-0164, Jan. 1995.

20. Hayder, M.E., and Turkel, E., "On Buffer Layers as Non-Reflecting Computational Boundaries," AIAA paper 96-0273, Jan. 1996.

21. Freund, J.B., "Proposed Inflow/Outflow Boundary Condition for Direct Computation of Aerodynamic Sound," AIAA Journal, Vol. 35, April 1997, pp. 740-742.

22. Berenger, J.P., "A Perfectly Matched Layer for the Absorption of Electromagnetic Waves," Journal of Computational Physics, Vol. 114, 1994, pp. 182-200.

23. Berenger, J.P., "Three Dimensional Perfectly Matched Layer for the Absorption of Electromagnetic Waves," Journal of Computational Physics, Vol. 127, 1996, pp. 363-379.

24. Hastings, F.D., Schneider, J.B. and Broschat, S.L., "Application of the Perfectly Matched layer (PML) Absorbing Boundary Condition to Elastic Wave Propagation," Journal Acoustical Society America, Vol. 100, Nov. 1996, pp. 3061-3069.

25. Hu, F.Q., "On Absorbing Boundary Conditions for Linearized Euler Equations by a Perfectly Matched Layer," Journal of Computational Physics, Vol. 129, 1996, pp. 201-219.

26. Hu, F.Q., "On Perfectly Matched Layer As An Absorbing Boundary Condition," AIAA Paper 96-1664, May 1996.

27. Hayder, M., Hu, F.Q., and Hussaini, Y.M., "Toward Perfectly Absorbing Boundary Conditions for Euler Equations," AIAA Paper 97-2075, June 1997.

28. Hu, F.Q., and Manthey, J.L., "Application of PML Absorbing Boundary Conditions to the Benchmark Problems of Computational Aeroacoustics," in Proceedings of the Second Computational Aeroacoustics Workshop on Benchmark Problems, ed. C.K.W.Tam and J.C. Hardin, 1997 (to be published as a NASA CP).

29. Tam, C.K.W., Webb, J.C., and Dong, Z., "A Study of the Short Wave Components in Computational Acoustics," Journal of Computational Acoustics, Vol. 1, Mar. 1993, pp. 1-30.

30. Giles, M.B., "Nonreflecting Boundary Conditions for Euler Equation Calculations," AIAA Journal, Vol. 28, Dec. 1990, pp. 2050-2058.

31. Atkins, H., and Casper, J., "Nonreflective Boundary Conditions for High-Order Methods," AIAA Journal, Vol. 32, Mar. 1994, pp. 512-518.

32. Colonius, T., "Numerically Nonreflecting Boundary and Interface Conditions," AIAA Paper 96-1661, May 1996.

33. Scott, J.N., Mankbadi, R.R., Hayder, M.E. and Hariharan, S.I., "Outflow Boundary Conditions for the Computational Analysis of Jet Noise," AIAA Paper 93-4366, Oct. 1993.

34. Kroner, D., "Absorbing Boundary Conditions for the Linearized Euler Equations in 2-D," Mathematics of Computation, Vol. 57, 1991, pp. 153-167.

35. Roe, P., "Remote Boundary Conditions for Unsteady Multidimensional Aerodynamic Computations," Computers and Fluids Journal, Vol. 17, 1989, pp. 221-231.

36. Hixon, D.R., Shih, S., and Mankbadi, R.R., "Evaluation of Boundary Conditions for Computational Aeroacoustics," AIAA Journal, Vol. 33, Nov. 1995, pp. 2006-2012.

37. Hayder, M.E., and Turkel, E., "Nonreflecting Boundary Conditions for Jet Flow Computations," AIAA Journal, Vol. 33, Dec. 1995, pp. 2264-2270.

38. Dong, T.Z., "A Set of Simple Radiation Boundary Conditions for Acoustics Computations in Nonuniform Mean Flows," AIAA Paper 96-0274, Jan. 1996.

39. Hardin, J.C., Ristorcelli, J.R., and Tam, C.K.W., ICASE/LaRC workshop on Benchmark Problems in Computational Aeroacoustics. NASA CP 3300, May 1995.

40. Tam, C.K.W., and Hardin, J.C. Second Computational Aeroacoustics workshop on Benchmark Problems (to be published as a NASA CP, 1997).

41. Tam, C.K.W. and Dong, Z., "Wall Boundary Conditions for High-Order Finite Difference Schemes in Computational Aeroacoustics," Theoretical and Computational Fluid Dynamics, Vol. 8, 1994, pp. 303-322.

42. Kurbatskii, K.A., and Tam, C.K.W., "Cartesian Boundary Treatment of Curved Walls for High-

13

Order Computational Aeroacoustics Schemes," AIAA Journal, Vol. 35, Jan. 1997, pp. 133–140.

43. Chung, C., and Morris, P.J. "Acoustic Scattering from Two and Three-Dimensional Bodies," Proceedings of the First Joint CEAS/AIAA Aeroacoustics Conference, June 1995, Munich, Germany, pp. 55–63.

44. Motsinger, R.E., and Kraft, R.E., "Design and Performance of Duct Acoustic Treatment", in Aeroacoustics of Flight Vehicles: Theory and Practice, ed. H.H. Hubbard, NASA RP–1258, Aug. 1991, Chapter 14.

45. Ozyoruk, Y., and Long, L.L., "A Time-Domain Implementation of Surface Acoustic Impedance Condition With and Without Flow," AIAA Paper 96–1663, May 1996.

46. Ozyoruk, Y., and Long, L.L., "Impedance Boundary Conditions for Time-Domain Computational Aeroacoustics Methods", AIAA Paper 97–0021, Jan. 1997.

47. Sullivan, D.M., "Frequency-Dependent FDTD Methods Using z Transform," IEEE Transactions on Antennas and Propagation, Vol. 40, Oct. 1992, pp. 1223–1230.

48. Penny, C., "Scattering From Coated Targets Using a Frequency-Dependent Impedance Boundary Condition in the Finite Difference Time-Domain Method, "Ph.D. Thesis, The Pennsylvania State University, University Park, May 1995.

49. Tam, C.K.W., and Auriault, L., "Time-Domain Impedance Boundary Conditions for Computational Aeroacoustics," AIAA Journal, Vol. 34, May 1996, pp. 917–923.

50. Tam, C.K.W., Kurbatskii, K. and Fang, J., "Numerical Boundary Conditions for Computational Aeroacoustics Benchmark Problems", in Proceedings of the Second Computational Aeroacoustics Workshop on Benchmark Problems, ed. C.K.W. Tam and J.C. Hardin, 1997 (to be published as a NASA CP).

51. Tam, C.K.W. and Dong, Z., "Radiation and Outflow Boundary Conditions for Direct Computation of Acoustic and Flow Disturbances in a Nonuniform Mean Flow," Journal of Computational Acoustics, Vol. 4, 1996, pp. 175–201.

52. Tam, C.K.W., "Supersonic Jet Noise," Annual Review of Fluid Mechanics, Vol. 27, 1995, pp. 17–43.

53. Tam, C.K.W., and Shen, H., "Numerical Simulation of the Jet Screech Phenomenon Using Computational Aeroacoustics Method," First AFOSR International Conference on Direct Numerical Simulation and Large Eddy Simulation. (Abstract submitted) Aug., 1997, Ruston, Louisiana.

54. Kendall, J.M., and Ahtye, W.F., "Noise Generation by a Lifting Wing/Flop Combination at Reynolds Numbers to $2.8x10^6$," AIAA Paper 80–0035, Jan. 1980.

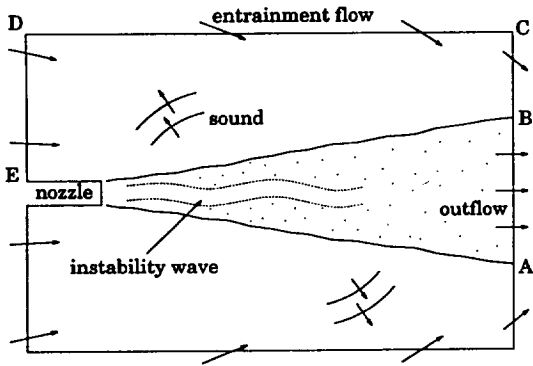55. Thies, A.T., Tam, C.K.W., and Reddy, N.N., Airframe Noise via Numerical Simulation," to be published.

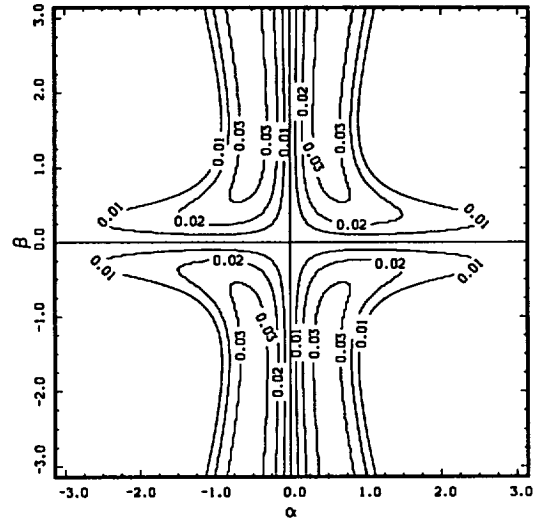Figure 1. The computation domain for numerical simulation of jet noise generation

Figure 2. The computation domain for numerical simulation of fan noise radiation from a jet engin inlet

Figure 3. Two dimensional computation domain with Perfectly Matched Layers as boundaries

Figure 4. Contours of the growth rate of the most unstable wave in the $\alpha - \beta$ plane. $M_x = 0.3$, $M_y = 0$, $\sigma = 1.5$
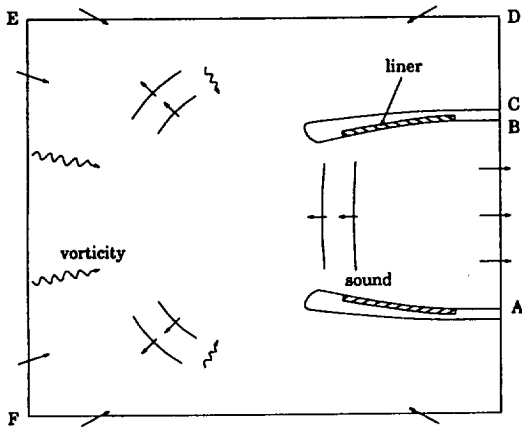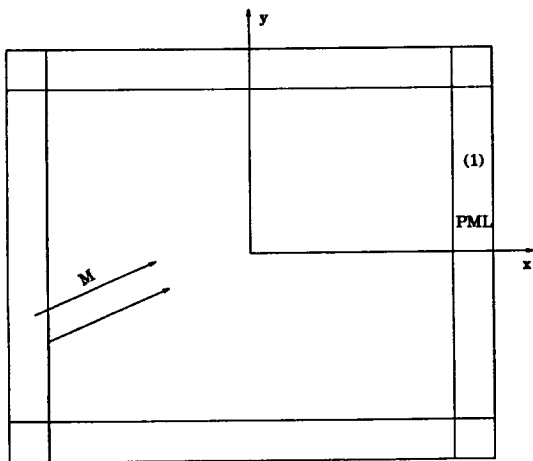

Figure 5. Contours of constant damping rate in the $\alpha - \beta$ plane.
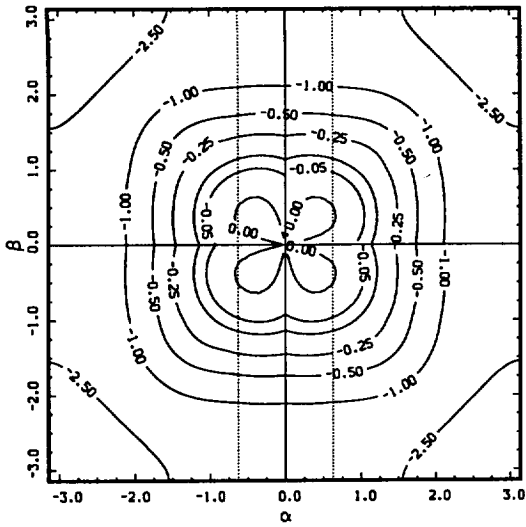
Figure 6. Contours of combined growth and damping rates for $R_\Delta = 0.46$
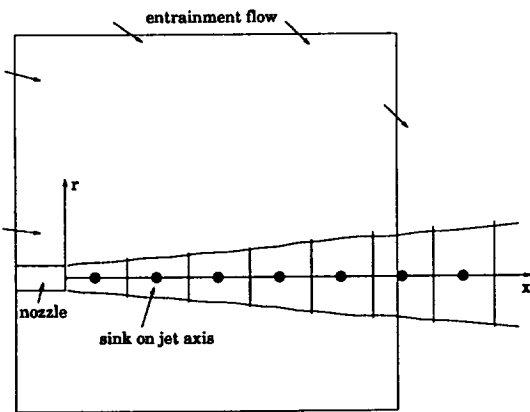
Figure 7. Determination of the entrainment flow of a supersonic jet by the point-sinks approximation
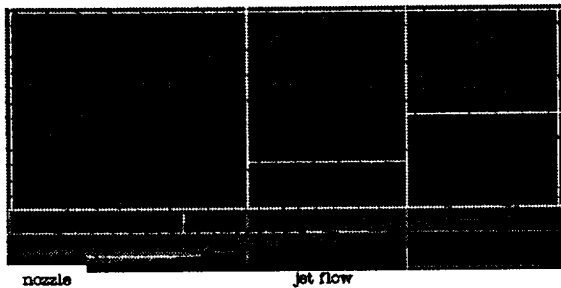
Figure 8. Computed streamlines of the entrainment flow around a supersonic screeching jet at $M = 1.13$
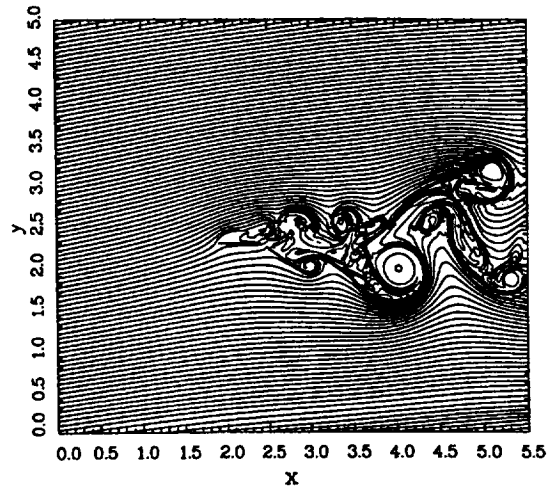

Figure 9. Streaklines of flow around a wing-flap combination at Mach 0.15 and 6 degrees angle of attack
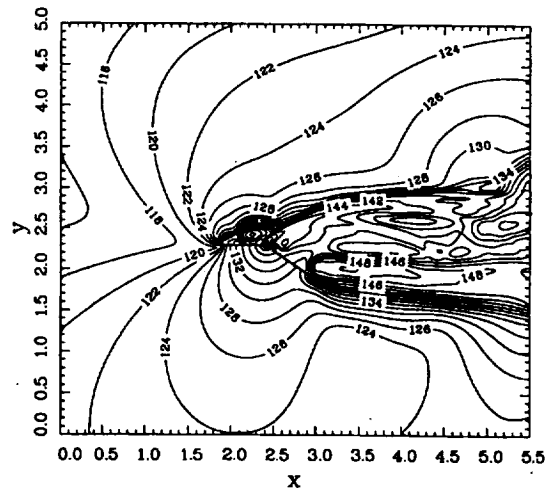

Figure 10. Sound-pressure-level contours obtained by numerical simulation of the flow around a wing-flap combination at Mach 0.15 and 6 degrees angle of attack

16

AIAA 98-0183

Perfectly Matched Layer for Linearized Euler
Equations in Open and Ducted Domains

C. K. W. Tam and L. Auriault
Florida State University
Tallahassee, FL

F. Cambuli
Universita degli Studi di Cagliari
Cagliari, Italy

36th Aerospace Sciences
Meeting & Exhibit
January 12–15, 1998 / Reno, NV

Perfectly Matched Layer as Absorbing Boundary Condition for the Linearized Euler Equations in Open and Ducted Domains[†]

Christopher K.W. Tam[*] and Laurent Auriault[**]
Department of Mathematics
Florida State University
Tallahassee, FL 32306-4510
tam@math.fsu.edu

Francesco Cambuli[***]
Dipartimento di Ingegneria Meccanica
Universita degli Studi di Cagliari
Piazza d'Armi
09123 Cagliari, Italy

Abstract

Recently, perfectly matched layer (PML) as an absorbing boundary condition has found widespread applications. The idea was first introduced by Berenger for electromagnetic waves computations. In this paper, it is shown that the PML equations for the linearized Euler equations support unstable solutions when the mean flow has a component normal to the layer. To suppress such unstable solutions so as to render the PML concept useful for this class of problems, it is proposed that artificial selective damping terms be added to the discretized PML equations. It is demonstrated that with a proper choice of artificial mesh Reynolds number, the PML equations can be made stable. Numerical examples are provided to illustrate that the stabilized PML performs well as an absorbing boundary condition. In a ducted environment, the wave mode are dispersive. It will be shown that the group velocity and phase velocity of these modes can have opposite signs. This results in a band of transmitted waves in the PML to be spatially amplifying instead of evanescent. Thus in a confined environment, PML may not be suitable as an absorbing boundary condition.

1. Introduction

Recently, Berenger[1,2] succeeded in formulating an absorbing boundary condition for computational

electromagnetics that has the unusual characteristic that when an outgoing disturbance impinges on the interface between the computation domain and the absorbing layer surrounding it, no wave is reflected back into the computation domain. In other words, all the outgoing disturbances are transmitted into the absorbing layer where they are damped out. Such a layer has come to be known as a perfectly matched layer (PML).

Since its initial development, PML has found widespread applications in elastic wave propagation[3], computational aeroacoustics and many other areas. Hu[4] was the first to apply PML to aeroacoustics problems governed by the linearized Euler equations; linearized over a uniform mean flow. He has since extended his work to nonuniform mean flow and for the fully nonlinear Euler equations[5]. Further applications of PML to acoustics problems including wavemodes in ducts can be found in the most recent works of Hu and coworkers[6,7]. In these references, examples are provided that indicate that high quality numerical solutions could be found with PML used as radiation or outflow boundary conditions.

In open unbounded domains, acoustic waves are nondispersive and propagate with the speed of sound relative to the local mean flow. Inside a duct, the situation is completely different. Acoustic waves are repeatedly reflected back by the confining walls. For ducts with parallel walls, the continuous reflection of the acoustic waves by the wall leads to the formation of coherent wave patterns called duct modes[8,9]. Unlike the open domain, duct modes are dispersive with phase and group velocities vary with axial wavenumber. Because of the dispersive nature of the duct modes many radiation boundary conditions that work well in open domains are known to be inappropriate for ducted environments. For this reason, Tam[10] in a recent review on numerical

boundary conditions for computational aeroacoustics, suggested that boundary condition for ducted environment be regarded as a category of its own.

There are three primary objectives in this work. First, we intend to show that in the presence of a mean flow normal to a PML, the standard PML equations of the linearized Euler equations support unstable solutions. Earlier Tam[10] had pointed out that the PML equations with mean flow have unstable solutions. However, he did not show that the existence of instabilities is due to the mean flow component normal to the layer. The origin and characteristics of these instabilities are investigated and analyzed. It is interesting to mention that in his earliest work, Hu[4] reported that his computation encountered numerical instability. But by applying numerical filtering, he was able to obtain stable solutions. In light of our finding, we believe that what Hu encountered was not instability of his numerical scheme but that his numerical solution inadvertently excited the intrinsic unstable solution of the PML equations. Not directly related to the instability of the PML equations, Abarbanel and Gottlieb[11] recently analyzed the electromagnetic PML equations. They concluded that the equations are only weakly well-posed.

Second, we will show that the instability is not very strong, namely, the growth rates are small. Also the instabilities are confined primarily to short waves. It is, therefore, possible to suppress the instabilities by the addition of artificial selective damping terms[12] to the discretized PML equations. It is important to point out that artificial selective damping eliminates mainly the short waves and has negligible effect on the long or the physical waves. Thus the addition of these damping terms does not effect the perfectly matched conditions of the PML.

Third, we will show that a perfectly matched layer may not be suitable as an absorbing boundary condition for waves in a ducted flow environment. The major difference between acoustic waves in an open domain and acoustic waves inside a duct is that in an unbounded region acoustic waves are nondispersive whereas duct modes are dispersive. It will be shown that in the presence of a mean flow the group and phase velocity of the duct modes can have opposite signs. Because of this, a band of transmitted waves will actually grow spatially instead of being damped in the PML. In other words, the PML equations do not damp these wave modes as absorbing boundary condition ought to do. The exception is when there is no mean flow in the duct. In this special case, all the transmitted waves are spatially damped.

In section 2, the use of PML for open domain problems is discussed. The stability of the PML governing equations are investigated. It will be shown that the addition of damping terms to form the PML equations can actually cause the vorticity and acoustic wave modes to become unstable. The splitting of the variables in formulating the PML equations leads to a higher order system of equations. This higher system supports extra solutions. These extra or spurious solutions are found to become unstable when the damping coefficient is large. Numerical examples are provided to illustrate the spread of the unstable solution from the PML back into the interior of the computation domain.

In section 3, the effect of the addition of artificial selective damping terms to the discretized PML equations is investigated. It is shown that with an appropriate choice of mesh Reynolds number, the unstable solutions of the PML equations can be suppressed. Numerical examples are given to demonstrate the effectiveness of the modified PML as a radiation/outflow boundary condition.

Section 4 deals with the theory and application of PML to ducted internal flow problems. An eigenvalue analysis is carried out to show the existence of a band of frequency for which the PML exerts no damping on the acoustic duct modes. These wave modes actually would grow in amplitude as they propagate through the PML. Numerical results are provided to illustrate the existence of this kind of amplifying ducted acoustic modes.

2. Open Domain Problems

Let us consider the use of PML as absorbing boundary condition for the solution of the linearized Euler equations (linearized over a uniform mean flow) in a two-dimensional open domain as shown in figure 1. We will use $\Delta x = \Delta y$ (the mesh size) as the length scale, a_0 (the sound speed) as the velocity scale, $\frac{\Delta x}{a_0}$ as the time scale, $\rho_0 a_0^2$ (where ρ_0 is the mean density) as the pressure scale. The dimensionless governing equations in the PML are formed by splitting the linearized Euler equations according to the spatial derivatives. An absorption term is added to each of the equations with spatial derivative in the direction normal to the layer. For example, for the PML on the right boundary of figure 1, the governing equations are[4],

$$\frac{\partial u_1}{\partial t} + \sigma u_1 + M_x \frac{\partial}{\partial x}(u_1 + u_2)$$

$$+ \frac{\partial}{\partial x}(p_1 + p_2) = 0$$

2

$$\frac{\partial u_2}{\partial t} + M_y \frac{\partial}{\partial y}(u_1 + u_2) = 0$$

$$\frac{\partial v_1}{\partial t} + \sigma v_1 + M_x \frac{\partial}{\partial x}(v_1 + v_2) = 0$$

$$\frac{\partial v_2}{\partial t} + M_y \frac{\partial}{\partial y}(v_1 + v_2) + \frac{\partial}{\partial y}(p_1 + p_2) = 0$$

$$\frac{\partial p_1}{\partial t} + \sigma p_1 + M_x \frac{\partial}{\partial x}(p_1 + p_2)$$

$$+ \frac{\partial}{\partial x}(u_1 + u_2) = 0$$

$$\frac{\partial p_2}{\partial t} + M_y \frac{\partial}{\partial y}(p_1 + p_2) + \frac{\partial}{\partial y}(v_1 + v_2) = 0$$

$$(1)$$

where M_x and M_y are the mean flow Mach numbers in the x and y directions. σ is the absorption coefficient.

Suppose we look for solutions with (x, y, t) dependence in the form $\exp[i(\alpha x + \beta y - \omega t)]$. It is easy to find from (1) that the dispersion relations of the PML equations are,

$$\left(1 - \frac{\alpha M_x}{\omega + i\sigma} - \frac{\beta M_y}{\omega}\right)^2 - \frac{\alpha^2}{(\omega + i\sigma)^2} - \frac{\beta^2}{\omega^2} = 0 \quad (2)$$

$$1 - \frac{\alpha M_x}{\omega + i\sigma} - \frac{\beta M_y}{\omega} = 0. \quad (3)$$

In the limit $\sigma \to 0$, (2) and (3) become the well-known dispersion relations of the acoustic and the vorticity waves of the linearized Euler equations.

2.1. Mean Flow Parallel to PML

Dispersion relations (2) and (3) behave very differently depending on whether there is any mean flow normal to the PML. When the mean flow is parallel to the layer; i.e., $M_x = 0$, the solutions are stable. This is easy to see from (3) for the vorticity wave. Physically, if the mean flow is parallel to the PML, the vorticity waves in the computation domain, being convected by the mean flow, cannot enter the layer and hence would not lead to unstable solution. To show that for $M_x = 0$ all the solutions of (2) are stable, a simple mapping will suffice. Rewrite (2) in the form

$$F \equiv (\omega - \beta M_y)^2 - \frac{\alpha^2 \omega^2}{(\omega + i\sigma)^2} = \beta^2. \quad (4)$$

Figure (2) shows the image of the upper-half ω-plane in the F plane. The upper-half ω-plane is mapped

into the entire F plane except for the slit ADC. But since β^2 is real and positive, for subsonic mean flow the point β^2 lies outside the image. Thus no value of ω in the upper-half ω-plane would satisfy equation (2) indicating that there is no unstable solution.

2.2. Unstable Solutions of the PML Equations

For $M_x \neq 0$, the PML equations support unstable solutions. It is to be noted that, unlike the original dispersion relation of the acoustic waves, equation (2) is a quadric equation in ω. It has two extra roots in addition to the two modified acoustic modes. For small σ, the two spurious roots are damped but one of the modified acoustic roots is unstable. For larger σ, numerical solutions indicate that one of the spurious roots becomes unstable. In any case, the equation splitting procedure and the addition of an absorption term, both are vital to the suppression of reflections at the interface between the computation domain and the PML, inadvertently, lead to instabilities.

For small σ, the roots of (2) and (3) can be found by perturbation. Let,

$$\omega^{(a)} = \omega_0^{(a)} + \sigma \omega_1^{(a)} + \sigma^2 \omega_2^{(a)} + \ldots \quad (5)$$

$$\omega^{(v)} = \omega_0^{(v)} + \sigma \omega_1^{(v)} + \sigma^2 \omega_2^{(v)} + \ldots \quad (6)$$

where the roots of (2) and (3) are designated by a superscript 'a' (for acoustic waves) and 'v' (for vorticity waves). Substitution of (5) and (6) into (2) and (3), it is straightforward to find,

$$\omega_0^{(a)} = \omega_+, \quad \omega_-, \quad 0, \quad 0 \quad (7)$$

where

$$\omega_\pm = (\alpha M_x + \beta M_y) \pm (\alpha^2 + \beta^2)^{\frac{1}{2}} \quad (8)$$

$$\omega_1^{(a)} = i \left[\frac{-\alpha^2 \mp \alpha M_x (\alpha^2 + \beta^2)^{\frac{1}{2}}}{\alpha^2 + \beta^2 \pm (\alpha M_x + \beta M_y)(\alpha^2 + \beta^2)^{\frac{1}{2}}} \right] \quad (9)$$

$$\omega_0^{(v)} = \alpha M_x + \beta M_y, \quad 0 \quad (9)$$

$$\omega_1^{(v)} = \frac{-i}{1 + (\frac{M_y}{M_x})(\frac{\beta}{\alpha})}. \quad (11)$$

Clearly if $\omega_1^{(a)}$ or $\omega_1^{(v)}$ has a positive imaginary part, the mode is unstable. It is easy to show, especially in the case $M_y = 0$, that there are always values of α and β such that $\omega_1^{(a)}$ of (10) is purely imaginary

3

and positive. Similarly, from (11) for $\frac{\beta}{\alpha} < 0$ and $|\frac{\beta}{\alpha}| > \frac{M_x}{M_y}$, $\omega_1^{(v)}$ is also purely positive imaginary. Thus the PML equations in the presence of a uniform flow with $M_x \neq 0$ support unstable solutions.

The unstable solutions of dispersion relations (2) and (3) can also be found numerically. For a given (α, β) the growth rates, ω_i, of the unstable solutions can be calculated in a straightforward manner. Figure (3) shows the ω_i contours of the most unstable solution of equation (2), the acoustic mode, in the $\alpha - \beta$-plane for the case $M_x = 0.3$, $M_y = 0.0$ and $\sigma = 1.5$. Figure 4 shows a similar plot for the vorticity wave mode (equation (3)). In these figures only the unstable regions are shown. It is clear that there are instability waves over a wide range of wavenumbers. Numerical results indicate that, in general, the unstable regions expand as the flow Mach number or the damping coefficient σ increases.

2.3. Numerical Examples

The nature and characteristics of the unstable waves associated with the acoustic mode and the vorticity mode are quite different. To illustrate the excitation of these unstable solutions in the PML by disturbances propagating or convecting from the interior computation domain, a series of numerical experiments has been carried out. Figure 5 shows the results of the case of a vorticity pulse convected into the PML when $M_x = 0.3$, $M_y = 0.2$ and $\sigma = 1.0$. The initial conditions for the pulse are (same as the initial conditions used by Tam & Webb[13])

$$p = \rho = 0$$

$$u = 0.04 y \exp\left[-(\ell n\, 2)\left(\frac{x^2 + y^2}{25}\right)\right] \qquad (10)$$

$$v = -0.04 x \exp\left[-(\ell n\, 2)\left(\frac{x^2 + y^2}{25}\right)\right].$$

The DRP time marching scheme[13] is used in the simulation. The PML region extends from $x = 20$ to the right boundary of the computation domain. At the outermost boundary, the boundary condition $p_1 = p_2 = \rho_1 = \rho_2 = u_1 = u_2 = v_1 = v_2 = 0$ are imposed. Plotted in figure 5 are contours of the u velocity component. Figure 5a shows the initial profile of the contours at $t = 0$. Figure 5b, at $t = 50$, reveals that there is damping of the vorticity pulse as it begins to enter the PML. This damping is the result of the built-in damping, σ, of the PML. Figure 5c, at a later time $t = 90$, shows the growth of

the excited unstable solution in the PML. Finally, figure 5d (at $t = 130$) shows the spread of the unstable solution back into the interior computation domain. Figure 6 gives the corresponding waveform of the vorticity wave pulse. Figure 6d clearly indicates that the spread of the unstable vorticity waves in the PML can quickly contaminate the entire computation domain.

Figures 7 and 8 are similar plots illustrating the excitation of the acoustic mode unstable solution in the PML. The Mach number and damping coefficient are $M_x = 0.5$, $M_y = 0.0$ and $\sigma = 1.5$. The initial disturbance consists of a pressure pulse given by,

$$p = \rho = \exp\left[-(\ell n\, 2)\left(\frac{x^2 + y^2}{9}\right)\right] \qquad (11)$$

$$u = v = 0.$$

The acoustic pulse generated by the initial disturbance propagates at a speed equal to the sound speed plus the flow velocity. Thus, the pulse leaves the small interior computation domain (50×50) very quickly. Figure 7a shows the pressure contours at $t = 140$. At this time, the acoustic pulse is gone. The contours are associated with the excited unstable waves of the acoustic mode. These unstable waves move at a slow speed. Figure 7b is at $t = 200$. On comparing figures 7a and 7b, it is evident that there is significant growth of the unstable waves. Upon reaching the outermost boundary of the computation domain the unstable waves are reflected back as short waves. This is illustrated in figure 7c. The reflected short waves propagate at ultrafast speed. They contaminate the computation domain in a short period of time as shown in figure 7d. Figure 8 shows the growth of the pressure waveform of the unstable acoustic mode waves in the PML before they reach the outer boundary of the computation domain. The measured growth rate has been found to agree with that calculated by the dispersion relation.

3. Development of a Stable PML

3.1. Artificial Selective Damping

To ensure practicality, the thickness of a PML would normally be limited to around 15 to 20 mesh spacings. For a PML with such a thickness, it is easy to show that if the transmitted wave from the computation domain is to be reduced by a factor of 10^5 in the presence of a subsonic mean flow, the damping coefficient σ of (1) should have a value of about

4

1.5. By solving the dispersion relations (2) and (3) numerically, it has been found that for $\sigma = 1.5$ the unstable wave solutions have only a modest rate of growth. Moreover, these waves, generally, have short wavelengths. Mild instabilities of this type can be effectively suppressed by the addition of artificial selective damping terms[12,14] to the discretized governing equations. The advantage of using artificial selective damping is that the damping is confined primarily to short waves. Thus, the perfectly matched condition is not adversely affected for the long waves (the physical waves) of the computation.

Consider the first equation of (1). Let (ℓ, m) be the spatial indices in the x- and y-directions. The semi-discretized form of this equation using the DRP scheme with artificial selective damping terms added to the right side is,

$$\frac{d}{dt}(u_1)_{\ell,m} + \sigma(u_1)_{\ell,m} + \sum_{j=-3}^{3} a_j [M_x(u_1 - u_2)_{\ell+j,m}]$$

$$+ (p_1 + p_2)_{\ell+j,m}] \qquad (12)$$

$$= -\frac{1}{R_\Delta} \sum_{j=-3}^{3} d_j [(u_1)_{\ell+j,m} + (u_2)_{\ell,j+m}]$$

where d_j's are the artificial selective damping coefficients[14] and $R_\Delta = a_\infty \frac{\Delta x}{\nu_a}$ is the artificial mesh Reynolds number. Terms similar to those on the right side of (12) are to be added to all the other discretized equations.

For the purpose of suppressing unstable solutions in the PML, we recommend the use of a damping curve with a slightly larger half-width then those given in ref. [14]. In this work, the following damping coefficients (half-width = 0.35π) are used.

$$d_0 = 0.3705630354$$

$$d_1 = d_{-1} = -0.2411788110$$

$$d_2 = d_{-2} = 0.0647184823 \qquad (13)$$

$$d_3 = d_{-3} = -0.0088211899.$$

The damping rate of the artificial selective damping terms can be found by taking the Fourier transform of the right side of (12) (see [12]). Let (α, β) be the transform variables in the (x, y)-plane. The rate of damping for wavenumber (α, β) is,

$$\text{damping rate} = \frac{1}{R_\Delta} D(\alpha, \beta) \qquad (14)$$

where

$$D(\alpha, \beta) = \sum_{j=-3}^{3} d_j \left(e^{ij\alpha} + e^{ij\beta} \right). \qquad (15)$$

Contours of the damping function $D(\alpha, \beta)$ in the $\alpha - \beta$-plane are shown in figure 9.

To demonstrate that suppression of the unstable solutions can be achieved by adding artificial selective damping terms to the discretized form of equation (1), let us consider the unstable solution with growth rate given by figure 3. On combining the growth rate of figure 3 and the damping rate of figure 9 with $R_\Delta = 1.421$, the resulting growth contours are shown in figure 10. Outside the dotted lines (wavenumber inside the vertical dotted lines corresponds to wavelengths too long to fit into a 15 mesh spacing PML) the combined effects result in damping of the waves. Thus all the instabilities of the PML equations are effectively suppressed.

3.2. Distributions of σ and R_Δ^{-1} in the PML

In the implementation of PML as an absorbing boundary condition, Hu[14] suggested letting σ vary spatially in the form,

$$\sigma = \sigma_m \left(\frac{d}{D} \right)^\lambda \qquad (16)$$

where D is the thickness of the PML, d is the distance from the interface with the interior domain and λ is a constant. With the inclusion of artificial selective damping, we have found that the use of a well-designed smooth distribution of σ and R_Δ^{-1} at the interface region is important if the perfectly matched condition is to be maintained in the finite difference form of the system of equations.

Figure 11 shows a distribution of σ and R_Δ^{-1} we found to work well with the 7-point stencil DRP scheme. The R_Δ^{-1} curve is zero for the first two mesh points closest to the interface. It attends its full value $(R_\Delta^{-1})_{max}$ at the 6th mesh point. A cubic spline curve is used in the transition region. With this arrangement, the first point that artificial damping occurs is the third point from the interface. This allows the use of the 7-point symmetric damping stencil in the PML except the last three points at the outer boundary. For these points, the 5-point and the 3-point stencil[14] should be used instead.

The σ curve begins with the value $\sigma = 0$ at the fifth mesh point from the interface. The full value σ_{max} is reached at 8 mesh points further away. Again, a cubic spline curve is used in the transition

5

region. The choice of starting the σ curve at the fifth point is to ensure that the R_Δ^{-1} curve has attained its full value when σ becomes nonzero.

3.3. Numerical Examples

To demonstrate the effectiveness of using artificial selective damping terms to suppress the instabilities of the PML equations, the numerical examples of section 2.3 are reconsidered here. Artificial damping is now included in the simulations. Figure 12 shows the u-contours of the vorticity waves ($M_x = 0.3$, $M_y = 0.2$, $\sigma_m = 1.0$, $(R_\Delta^{-1})_{max} = 1.0$) as they are convected from the interior domain to the PML. The vorticity wave packet is steadily damped. No sign of unstable waves of the type shown in figure 5 is detected. Figure 13 shows the corresponding waveform of u at a few selected times. It is clear that the pulse is damped continuously once it propagates into the PML. The case of the acoustic disturbance has also been repeated with similar results. Based on these findings, it is concluded that a stable PML can be developed by the inclusion of artificial selective damping. Such a PML performs very effectively as an absorbing boundary condition in an open domain.

4. PML in Ducted Environments

We will now consider the use of PML inside a circular duct of radius R. Dimensionless variables with respect to length scale R, velocity scale a_t (speed of sound at $r = R$), time scale $\frac{R}{a_t}$, density scale ρ_t (mean density at $r = R$) and pressure scale $\rho_t a_t^2$ will be used. The velocity components in the (x, r, ϕ) directions of a cylindrical coordinate system are denoted by (u, v, w). For an inviscid compressible flow, the most general mean flow (designated by an overbar) is

$$\bar{u} = \bar{u}(r), \quad \bar{v} = 0, \quad \bar{w} = \bar{w}(r), \quad \bar{p} = \bar{p}(r)$$

$$\bar{p} = -\int_r^1 \frac{\bar{\rho}\,\bar{w}^2}{r}\,dr + p_0. \tag{17}$$

Small amplitude disturbances superimposed on mean flow (17) are governed by the linearized Euler equations. They are,

$$\frac{\partial \rho}{\partial t} + \frac{1}{r}\frac{\partial}{\partial r}(\bar{\rho}\,vr) + \frac{\bar{w}}{r}\frac{\partial \rho}{\partial \phi} + \bar{u}\frac{\partial \rho}{\partial x}$$

$$+ \bar{\rho}\left(\frac{1}{r}\frac{\partial w}{\partial \phi} + \frac{\partial u}{\partial x}\right) = 0 \tag{18a}$$

$$\bar{\rho}\left[\frac{\partial v}{\partial t} + \bar{u}\frac{\partial v}{\partial x} + \frac{\bar{w}}{r}\frac{\partial v}{\partial \phi} - \frac{2\,\bar{w}\,w}{r}\right] - \rho\frac{\bar{w}^2}{r}$$

$$= -\frac{\partial p}{\partial r} \tag{18b}$$

$$\bar{\rho}\left[\frac{\partial w}{\partial t} + \bar{u}\frac{\partial w}{\partial x} + v\frac{d\bar{w}}{dr} + \frac{\bar{w}}{r}\frac{\partial w}{\partial \phi} + \frac{\bar{w}\,v}{r}\right]$$

$$= -\frac{1}{r}\frac{\partial p}{\partial \phi} \tag{18c}$$

$$\bar{\rho}\left[\frac{\partial u}{\partial t} + \bar{u}\frac{\partial u}{\partial x} + v\frac{d\bar{u}}{dr} + \frac{\bar{w}}{r}\frac{\partial u}{\partial \phi}\right] = -\frac{\partial p}{\partial x} \tag{18d}$$

$$\frac{\partial p}{\partial t} + \bar{u}\frac{\partial p}{\partial x} + \frac{\bar{w}}{r}\frac{\partial p}{\partial \phi} + \frac{\bar{\rho}\,\bar{w}^2}{r}v$$

$$+ \gamma\bar{p}\left[\frac{1}{r}\frac{\partial vr}{\partial r} + \frac{1}{r}\frac{\partial w}{\partial \phi} + \frac{\partial u}{\partial x}\right] = 0 \tag{18e}$$

where γ is the ratio of specific heats. The boundary condition at the duct wall is

$$r = 1, \quad v = 0. \tag{19}$$

Solutions of (18) and (19) representing propagating wave modes in the duct may be written in the form,

$$\begin{bmatrix} \rho \\ u \\ v \\ w \\ p \end{bmatrix} = \mathrm{Re}\left\{ \begin{bmatrix} \tilde{\rho}(r) \\ \tilde{u}(r) \\ \tilde{v}(r) \\ \tilde{w}(r) \\ \tilde{p}(r) \end{bmatrix} \exp[i(kx + m\phi - \omega t)] \right\}. \tag{20}$$

Substitution of (20) into (18) and (19) leads to the following eigenvalue problem.

$$\tilde{\rho} + \frac{i}{\omega r}\frac{d}{dr}(\bar{\rho}\,\tilde{v}\,r) - \frac{m\,\bar{w}}{\omega r}\tilde{\rho} - \frac{k\,\bar{u}}{\omega}\tilde{\rho}$$

$$- \bar{\rho}\left(\frac{m}{\omega r}\tilde{w} + \frac{k}{\omega}\tilde{u}\right) = 0 \tag{21a}$$

$$\bar{\rho}\left[\left(1 - \frac{k}{\omega}\bar{u} - \frac{m\,\bar{w}}{\omega r}\right)\tilde{v} - i\frac{2\,\bar{w}\,\tilde{w}}{\omega r}\right] - \frac{i\,\tilde{\rho}\,\bar{w}^2}{\omega r}$$

$$= -\frac{i}{\omega}\frac{d\tilde{p}}{dr} \tag{21b}$$

$$\bar{\rho}\left[\left(1 - \frac{k}{\omega}\bar{u} - \frac{m\,\bar{w}}{\omega r}\right)\tilde{w} + \frac{i}{\omega}\tilde{v}\frac{d\bar{w}}{dr} + \frac{i\,\bar{w}}{\omega r}\tilde{v}\right]$$

6

$$= \frac{m}{\omega r} \tilde{p} \qquad (21c)$$

$$\bar{\rho}\left[\left(1 - \frac{k}{\omega}\bar{u} - \frac{m\,\bar{w}}{\omega r}\right)\tilde{u} + \frac{i}{\omega}\tilde{v}\frac{d\bar{u}}{dr}\right] = \frac{k}{\omega}\tilde{p} \quad (21d)$$

$$\left(1 - \frac{k\,\bar{u}}{\omega} - \frac{m\,\bar{w}}{\omega r}\right)\tilde{p} + \frac{i}{\omega}\frac{\bar{\rho}\,\bar{w}^2}{r}\tilde{v}$$

$$+ \gamma\bar{p}\left[\frac{i}{\omega r}\frac{d(\tilde{v}\,r)}{dr} - \frac{m}{\omega r}\tilde{w} - \frac{k}{\omega}\tilde{u}\right] = 0 \quad (21e)$$

$$r = 1, \quad \tilde{v} = 0 \qquad (22)$$

For a given azimuthal mode number m and frequency ω, k (the wavenumber) is the eigenvalue. Corresponding to an eigenvalue is an eigenvector $[\tilde{\rho}, \tilde{u}, \tilde{v}, \tilde{w}, \tilde{p}]$, which describes the radial profile of the wave mode.

4.1. Perfectly Matched Condition in Ducted Flows

Suppose a perfectly matched layer is to be set up as a termination boundary of a computation domain inside a duct. By splitting the variables; e.g., $\rho = \rho_1 + \rho_2$, etc. in the standard manner, the PML equations corresponding to the linearized Euler equations ((18a) to (18e)) are,

$$\frac{\partial\rho_1}{\partial t} + \frac{1}{r}\frac{\partial}{\partial r}[\bar{\rho}(v_1+v_2)r] + \frac{\bar{w}}{r}\frac{\partial(\rho_1+\rho_2)}{\partial\phi}$$

$$+ \frac{\bar{\rho}}{r}\frac{\partial(w_1+w_2)}{\partial\phi} = 0 \qquad (23a)$$

$$\frac{\partial\rho_2}{\partial t} + \sigma\rho_2 + \bar{u}\frac{\partial(\rho_1+\rho_2)}{\partial x}$$

$$+ \bar{\rho}\frac{\partial(u_1+u_2)}{\partial x} = 0 \qquad (23b)$$

$$\bar{\rho}\left[\frac{\partial v_1}{\partial t} + \frac{\bar{w}}{r}\frac{\partial(v_1+v_2)}{\partial\phi} - \frac{2\,\bar{w}(w_1+w_2)}{r}\right]$$

$$- (\rho_1+\rho_2)\frac{\bar{w}^2}{r} = -\frac{\partial}{\partial r}(p_1+p_2) \qquad (23c)$$

$$\bar{\rho}\left[\frac{\partial v_2}{\partial t} + \sigma v_2 + \bar{u}\frac{\partial(v_1+v_2)}{\partial x}\right] = 0 \qquad (23d)$$

$$\bar{\rho}\left[\frac{\partial w_1}{\partial t} + (v_1+v_2)\frac{d\bar{w}}{dr} + \frac{\bar{w}}{r}\frac{\partial(w_1+w_1)}{\partial\phi}\right.$$

$$\left. + \frac{\bar{w}}{r}(v_1+v_2)\right] = -\frac{1}{r}\frac{\partial(p_1+p_2)}{\partial\phi} \qquad (23e)$$

$$\bar{\rho}\left[\frac{\partial w_2}{\partial t} + \sigma w_2 + \bar{u}\frac{\partial(w_1+w_2)}{\partial x}\right] = 0 \qquad (23f)$$

$$\bar{\rho}\left[\frac{\partial u_1}{\partial t} + (v_1+v_2)\frac{d\bar{u}}{dr} + \frac{\bar{w}}{r}\bar{u}\frac{\partial(u_1+u_2)}{\partial\phi}\right]$$

$$= 0 \qquad (23g)$$

$$\bar{\rho}\left[\frac{\partial u_2}{\partial t} + \sigma u_2 + \bar{u}\frac{\partial(u_1+u_2)}{\partial x}\right]$$

$$= -\frac{\partial(p_1+p_2)}{\partial x} \qquad (23h)$$

$$\frac{\partial p_1}{\partial t} + \frac{\bar{w}}{r}\frac{\partial(p_1+p_2)}{\partial\phi} + \frac{\bar{\rho}\,\bar{w}^2}{r}(v_1+v_2)$$

$$+ \gamma\bar{p}\left[\frac{1}{r}\frac{\partial r(v_1+v_2)}{\partial r} + \frac{1}{r}\frac{\partial(w_1+w_2)}{\partial\phi}\right]$$

$$= 0 \qquad (23i)$$

$$\frac{\partial p_2}{\partial t} + \sigma p_2 + \bar{u}\frac{\partial(p_1+p_2)}{\partial x} + \gamma\bar{p}\frac{\partial(u_1+u_2)}{\partial x}$$

$$= 0 \qquad (23j)$$

where σ is the damping coefficient in the PML. The boundary condition is

$$r = 1, \qquad v_1 + v_2 = 0. \qquad (24)$$

In the PML, the duct modes are represented by solutions of the form (similar to (20)),

$$\rho_1(r,\phi,x,t) = \text{Re}\left[\hat{\rho}_1(r)e^{i(\kappa x + m\phi - \omega t)}\right], \qquad (25)$$

etc., where κ is the wavenumber. On substituting (25) into (23) and (24) and on defining

$$\hat{\rho} = \hat{\rho}_1 + \hat{\rho}_2$$

$$\hat{u} = \hat{u}_1 + \hat{u}_2$$

$$\hat{v} = \hat{v}_1 + \hat{v}_2 \qquad (26)$$

$$\hat{w} = \hat{w}_1 + \hat{w}_2$$

$$\hat{p} = \hat{p}_1 + \hat{p}_2$$

7

it is straightforward to find that the duct modes in the PML are given by the solutions of the following eigenvalue problem.

$$\widehat{p} + \frac{i}{\omega r}\frac{d}{dr}(\overline{p}\,\widehat{v}\,r) - \frac{m\,\overline{w}}{\omega r}\widehat{p} - \frac{\kappa\,\overline{u}}{\omega + i\sigma}\widehat{p}$$

$$- \overline{p}\left(\frac{m}{\omega r}\widehat{w} + \frac{\kappa}{\omega + i\sigma}\widehat{u}\right) = 0 \qquad (27a)$$

$$\overline{p}\left[\left(1 - \frac{\kappa}{\omega + i\sigma}\overline{u} - \frac{m\,\overline{w}}{\omega r}\right)\widehat{v} - i\frac{2\,\overline{w}\,\widehat{w}}{\omega r}\right]$$

$$- \frac{i\,\overline{p}\,\overline{w}^2}{\omega r} = -\frac{i}{\omega}\frac{d\widehat{p}}{dr} \qquad (27b)$$

$$\overline{p}\left[\left(1 - \frac{\kappa}{\omega + i\sigma}\overline{u} - \frac{m\,\overline{w}}{\omega r}\right)\widehat{w} + \frac{i}{\omega}\widehat{v}\frac{d\overline{w}}{dr}\right.$$

$$\left. + \frac{i\,\overline{w}}{\omega r}\widehat{v}\right] = \frac{m}{\omega r}\widehat{p} \qquad (27c)$$

$$\overline{p}\left[\left(1 - \frac{\kappa}{\omega + i\sigma}\overline{u} - \frac{m\,\overline{w}}{\omega r}\right)\widehat{u}\right.$$

$$\left. + \frac{i}{\omega}\widehat{v}\frac{d\overline{u}}{dr}\right] = \frac{\kappa}{\omega + i\sigma}\widehat{p} \qquad (27d)$$

$$\left(1 - \frac{\kappa\,\overline{u}}{\omega + i\sigma} - \frac{m\,\overline{w}}{\omega r}\right)\widehat{p} + \frac{i}{\omega}\frac{\overline{p}\,\overline{w}^2}{r}\widehat{v}$$

$$+ \gamma\overline{p}\left[\frac{i}{\omega r}\frac{d(\widehat{v}\,r)}{dr} - \frac{m}{\omega r}\widehat{w} - \frac{\kappa}{\omega + i\sigma}\widehat{u}\right]$$

$$= 0. \qquad (27e)$$

The boundary condition is

$$r = 1, \qquad \widehat{v} = 0. \qquad (28)$$

The eigenvalue is κ. On comparing eigenvalue problem (21) and (22) with eigenvalue problem (27) and (28), it is immediately clear that they are the same if $\frac{k}{\omega}$ in (21) is replaced by $\frac{\kappa}{\omega + i\sigma}$. Thus the eigenvalues are related by

$$\kappa = k\left(1 + \frac{i\sigma}{\omega}\right). \qquad (29)$$

On the other hand, the eigenvectors are identical. The fact that the eigenvectors of a duct mode in the interior region of the computation domain is the same as that in the PML assures that there is perfect matching. That is, a propagating duct mode incident on the PML will be totally transmitted into the PML without reflection. If the mean flow is nonuniform, some of the duct modes may involve Kelvin-Helmholtz or other types of flow instability waves. However, the perfectly matched condition is still valid for these waves.

4.2. The Case of Uniform Mean Flow

From (25) and (29), the transmitted wave mode has the form

$$[\widehat{p}(r), \widehat{u}(r), \widehat{v}(r), \widehat{w}(r), \widehat{p}(r)]\, e^{i[k(1 + \frac{i\sigma}{\omega})x + m\phi - \omega t]}. \qquad (30)$$

If the wave mode is nondispersive, then $\frac{k}{\omega}$, the inverse of the phase velocity, is positive for waves propagating in the x-direction and negative in the opposite direction. For these nondispersive waves, the transmitted waves are spatially damped; a condition needed by the PML if it is to serve as an absorbing boundary condition. However, inside a duct, the wave modes are dispersive. The direction of propagation is given by the group velocity $\frac{d\omega}{dk}$. We will now show that in the presence of a uniform mean flow there is a band of acoustic duct modes for which the group velocity and the phase velocity have opposite signs. Therefore, for this band of waves, the transmitted waves would grow spatially instead of being damped.

By eliminating all the other variables in favor of $\widetilde{p}(r)$, it is straightforward to find, in the case of a uniform mean flow of Mach number M, (21) and (22) reduce to the following simple eigenvalue problem.

$$\frac{d^2\widetilde{p}}{dr^2} + \frac{1}{r}\frac{d\widetilde{p}}{dr} + \left[(\omega - Mk)^2 - k^2 - \frac{m^2}{r^2}\right]\widetilde{p} = 0 \qquad (31)$$

$$r = 1, \qquad \frac{d\widetilde{p}}{dr} = 0. \qquad (32)$$

The eigenfunction is

$$\widetilde{p} = J_m(\lambda_{mn}r) \qquad (33)$$

where $J_m(\ )$ is the mth order Bessel function and λ_{mn} is the nth root of

$$J_m'(\lambda_{mn}) = 0. \qquad (34)$$

By substitution of (33) into (31), it is found that the dispersion relation or eigenvalue equation for the $(m, n)^{\text{th}}$ acoustic duct mode is

$$(\omega - Mk)^2 - k^2 = \lambda_{mn}^2. \qquad (35)$$

8

The axial wavenumber of the mode at frequency ω are given by the solution of (35). They are,

$$k_{\pm} = \frac{-\omega M \pm [\omega^2 - (1 - M^2)\lambda_{mn}^2]^{\frac{1}{2}}}{(1 - M^2)}. \qquad (36)$$

The group velocity of the duct mode may be determined by implicit differentiation of (35). This gives,

$$\frac{d\omega}{dk} = \frac{\pm[\omega^2 - (1 - M^2)\lambda_{mn}^2]^{\frac{1}{2}}(1 - M^2)}{\omega \mp M[\omega^2 - (1 - M^2)\lambda_{mn}^2]^{\frac{1}{2}}}. \qquad (37)$$

In (37), the upper sign corresponds to $k = k_+$ and the lower sign corresponds to $k = k_-$. For subsonic mean flow, clearly $\frac{d\omega}{dk} > 0$ for $k = k_+$ and $\frac{d\omega}{dk} < 0$ for $k = k_-$. Therefore, the downstream propagating waves have wavenumber given by $k = k_+$, while the upstream propagating waves have wavenumber equal to k_-.

From (37), it is easy to show that for $(1 - M^2)^{\frac{1}{2}}\lambda_{mn} < \omega < \lambda_{mn}$ the phase velocity $\frac{k_+}{\omega}$ is negative although the group velocity is positive. According to (29), for waves in this frequency band, the transmitted wave in the PML will amplify spatially. This renders the PML useless as an absorbing layer except for $M = 0$. In the absence of a mean flow normal to the PML ($M = 0$), k_+ will not be negative by (36). Thus, the transmitted waves in the PML are evanescent. For this special condition, the PML can again be used as an absorbing boundary condition.

4.3. Numerical Examples

To demonstrate that a PML in a ducted environment actually supports a band of amplifying wave modes, a series of numerical simulations has been carried out. In the simulations, a uniform mesh with $\Delta x = \Delta r = 0.04$ covering the entire computation domain from $x = -6.0$ to $x = 12.0$ is used. The PML in the upstream direction begins at $x = -3.0$ and extends to $x = -6.0$. In the downstream direction, the PML occupies the region from $x = 3.0$ to $x = 12.0$. The dimensionless damping constant (nondimensionalized by $\frac{a_\infty}{R}$) σ is set equal to 25.0. The results of two simulations, one with a mean flow Mach number 0.4, the other with no mean flow are reported below.

For convenience, only the axisymmetric duct modes are considered. The computation uses the 7-point stencil DRP scheme[13]. The acoustic disturbances in the computation domain is initiated by a pressure pulse located at $x = 0$ and $r = 0.5$. The

initial condition is,

$$t = 0, \quad u = v = 0,$$

$$p = \rho = \exp\left[-(\ell n\, 2)\frac{(x^2 + (r - 0.5)^2)}{16}\right]. \qquad (38)$$

Figure 14 shows the time evolution of the acoustic disturbance inside the computation domain at $M = 0.4$. Specifically, the pressure waveforms along the line $r = 0.38$ are shown at $t = 10, 13, 15$ and 16. As can be seen, once the pressure pulse is released, it spreads out and propagates upstream and downstream. Figure 14a indicates that at time $t = 10$ the front of the acoustic disturbance has just entered the PML in the downstream direction. There is no evidence of wave reflection at the interface between the PML and the interior computation domain. The transmitted wave grows spatially as shown in figure 14b. The amplitude of the transmitted wave increases steadily as they propagate across the PML. This is shown in figures 14c and 14d. When the amplified waves reach the outermost boundary of the PML, large amplitude spurious waves are reflected back. This quickly contaminates the entire computation domain.

Figure 15 shows the same simulation except that there is no mean flow. In the absence of a mean flow, the PML acts as an absorbing layer. Figure 15a shows the entry of the acoustic pulse into the downstream PML. Figures 15b to 15d show the damping of the acoustic pulse in time in the PML. The slowest components to decay are the long waves. This is in agreement with the analysis of the previous section.

5. Concluding Remarks

In this paper, we have shown that the application of PML as an absorbing boundary condition for the linearized Euler equations works well as long as there is no mean flow in the direction normal to the layer. For open domain problems, the PML equations, in the presence of a subsonic mean flow normal to the layer, support unstable solutions. The growth rate of the unstable solutions is, however, not large. These unstable solutions can, generally, be suppressed by the addition of artificial selective damping. In the case of a ducted environment, we find that because of the highly dispersive nature of the duct modes, a band of the transmitted waves in the PML amplifies instead of being damped. This seemingly renders the PML totally ineffective as an absorbing boundary condition.

9

One of the important advantages of using an absorbing boundary condition instead of other numerical boundary treatments is that the boundary of the computation domain may be put much closer to the source of disturbances. In this way, a smaller computation domain may be used in a numerical simulation. For open domains, such an absorbing boundary condition can be developed by the use of PML with artificial selective damping terms. Unfortunately, the same is not possible for internal ducted flow. An effective numerical anechoic termination for ducted domains has yet to be developed.

Acknowledgement

References

1. J.P. BERENGER, A perfectly matched layer for the absorption of electromagnetic waves, J. Comput. Phys. **114**, 185 (1994).

2. J.P. BERENGER, Three dimensional perfectly matched layer for the absorption of electromagnetic waves, J. Comput. Phys. **127**, 363 (1996).

3. F.D. HASTINGS, J.B. SCHNEIDER AND S.L. BROSCHAT, Application of the perfectly matched layer (PML) absorbing boundary condition to elastic wave propagation, J. Acoust. Soc. Amer. **100**, 3061 (1996).

4. F.Q. HU, On absorbing boundary conditions for linearized Euler equations by a perfectly matched layer, J. Comput. Phys. **129**, 201 (1996).

5. F.Q. HU, On perfectly matched layer as an absorbing boundary condition, AIAA paper 96-1664 (1996).

6. M. HAYDER, F.Q. HU, AND Y.M. HUSSAINI, Toward perfectly matched boundary conditions for Euler equations, AIAA paper 97-2075 (1997).

7. F.Q. HU AND J.L. MANTHEY, Application of PML absorbing boundary conditions to the benchmark problems of computational aeroacoustics, Proc. Second Comput. Aeroacoustics Workshop on Benchmark Problems, NASA CP-3352, 119 (1997).

8. P.M. MORSE AND K.U. INGARD, Theoretical Acoustics (McGraw Hill, New York, 1968).

9. W. EVERSMAN, Theoretical models for duct acoustic propagation and radiation, Chapter 13, pp. 101-163, in Aeroacoustics of Flight Vehicles: Theory and Practice, Vol. 2, NASA RP-1258 (1991).

10. C.K.W. TAM, Advances in numerical boundary conditions for computational aeroacoustics, AIAA Paper 97-1774 (1997), to appear in J. Comput. Acoustics.

11. S. ABARBANEL AND D. GOTTLIEB, A mathematical analysis of the PML method, J. Comput. Phys. **134**, 357 (1997).

12. C.K.W. TAM, J.C. WEBB AND Z. DONG, A study of the short wave components in computational acoustics, J. Comput. Acoustics **1**, 1 (1993).

13. C.K.W. TAM AND J.C. WEBB, Dispersion-Relation-Preserving finite difference schemes for computational acoustics, J. Comput. Phys. **107**, 262 (1993).

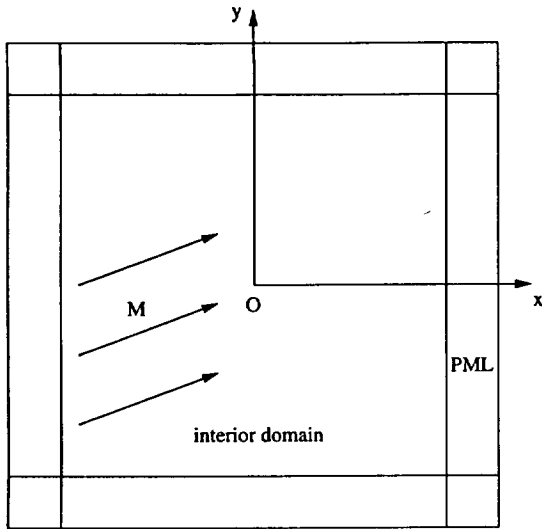14. C.K.W. TAM, Computational Aeroacoustics: Issues and Methods, AIAA J. **33**, 1788 (1995).

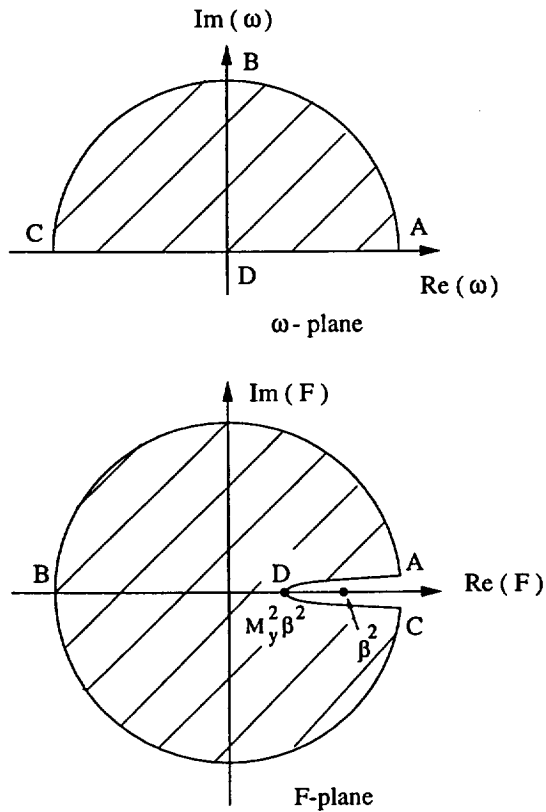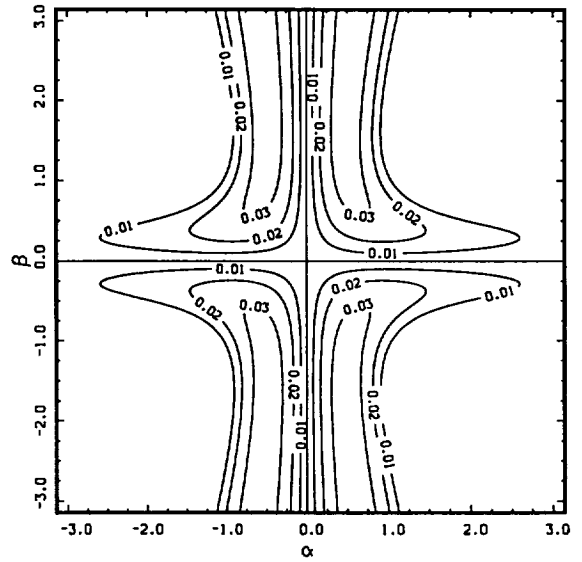Figure 1. Two dimensional computation domain with Perfectly Matched Layers as boundaries.

Figure 3. Contours of the growth rate of the most unstable wave (acoustic mode) in the $\alpha - \beta$ plane. $M_x = 0.3$, $M_y = 0.0$, $\sigma = 1.5$.
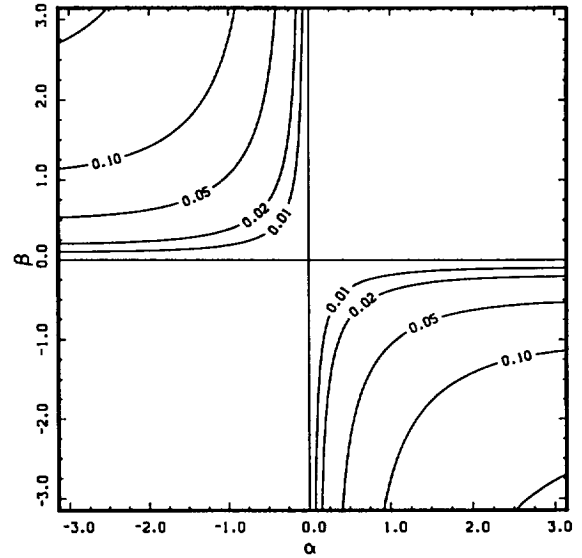

Figure 2. The image of the upper half ω-plane in the F-plane.

Figure 4. Contours of the growth rate of the most unstable vorticity wave in the $\alpha - \beta$ plane. $M_x = 0.3$, $M_y = 0.2$, $\sigma = 1.0$.
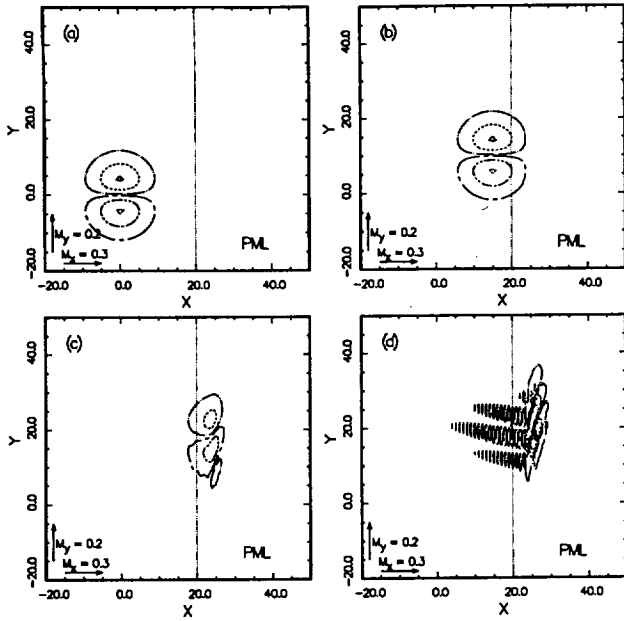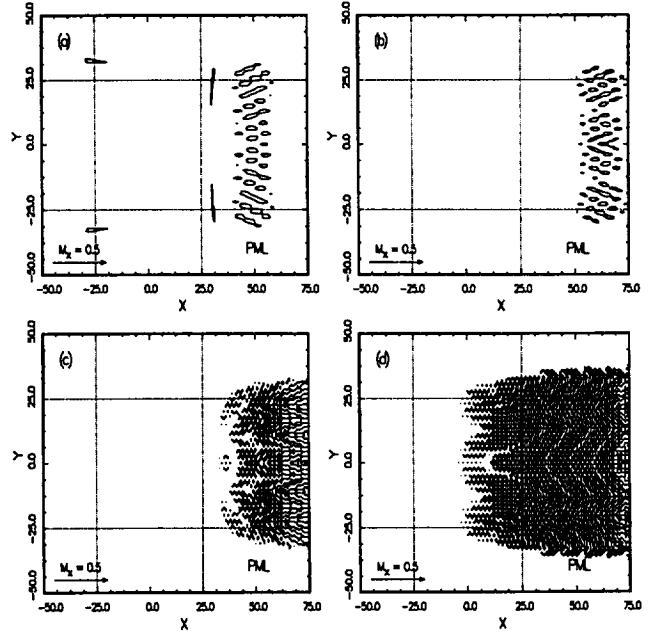
11

Figure 5. Numerical simulation showing the generation and propagation of unstable vorticity-mode waves in the PML. $M_x = 0.3$, $M_y = 0.2$, $\sigma_m = 1.0$. (a) $t = 0$, (b) $t = 50$, (c) $t = 90$, (d) $t = 130$. Contours of the u velocity component. ———— 0.1, – – – – – 0.05, — · — 0.01, — – — -0.01, – – —— -0.05, ········ -0.1.

Figure 7. Numerical simulation showing the generation and propagation of unstable acoustic-mode waves in the PML. $M_x = 0.5$, $M_y = 0.0$, $\sigma_m = 1.5$. Contours of pressure.
(a) $t = 140$, ——— $p = 10^{-4}$ (b) $t = 200$, ——— $p = 5. \ 10^{-3}$
(c) $t = 260$, ——— $p = 5. \ 10^{-2}$ (d) $t = 300$, ——— $p = 5. \ 10^{-2}$

Figure 6. Waveforms of u showing the generation of unstable vorticity-mode waves excited by vorticity waves convected from the interior computation domain to the PML and the subsequent contamination of the interior computation domain. $M_x = 0.3$, $M_y = 0.2$, $\sigma_m = 1.0$.
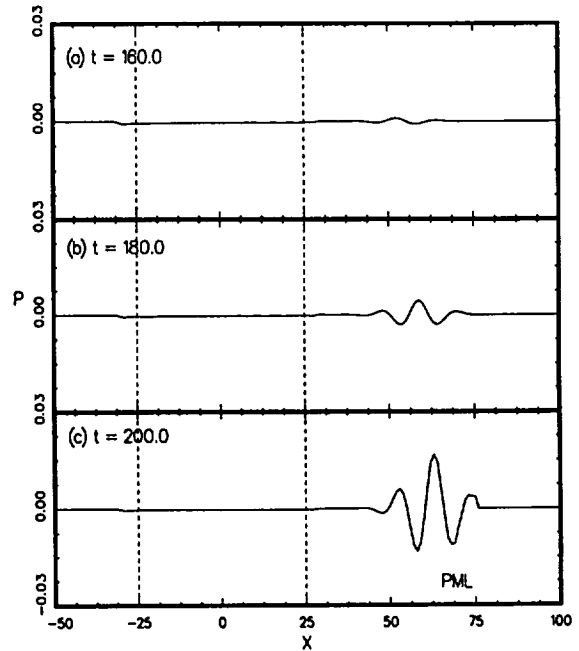

Figure 8. Waveforms of pressure along $y = 0$ showing the generation of unstable acoustic-mode waves in the PML excited by acoustic disturbances from the computation domain. $M_x = 0.5$, $M_y = 0.0$, $\sigma_m = 1.5$.
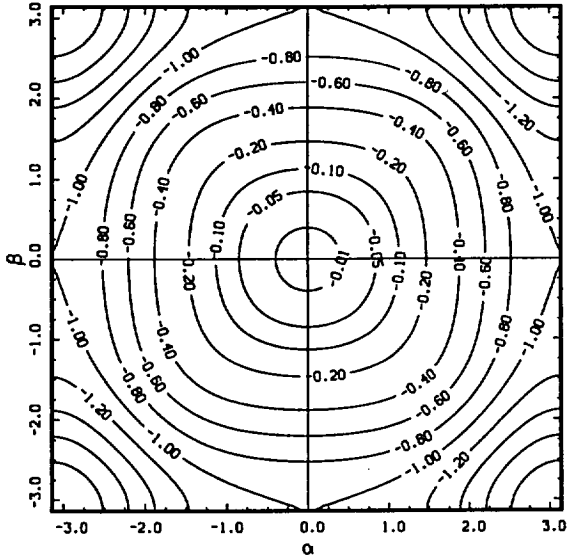
12

Figure 9. Contours of constant $D(\alpha, \beta)$ in the $\alpha - \beta$ plane. Damping coefficients d_j's are given by (13).

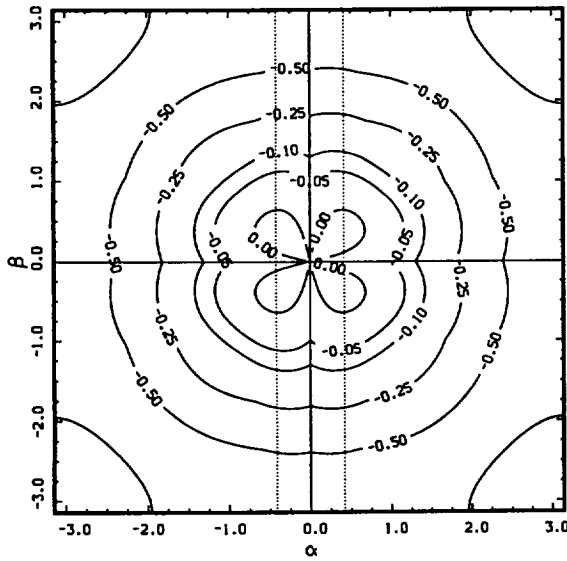Figure 11. Distributions of σ and R_Δ^{-1} in a 20 mesh spacings PML.

Figure 10. Contours of combined growth and damping rates. $M_x = 0.3$, $M_y = 0.0$, $\sigma = 1.5$, $R_\Delta = 1.42$. Damping coefficients d_j's are given by (13).
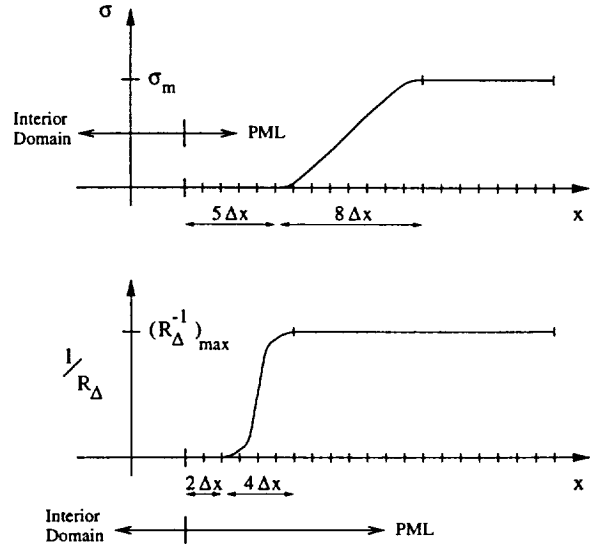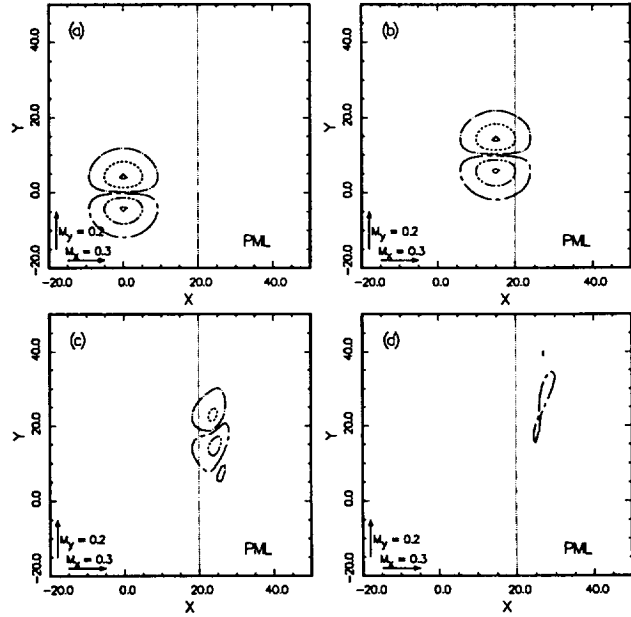

Figure 12. Damping of a vorticity wave packet in the PML including artificial selective damping terms. $M_x = 0.3$, $M_y = 0.2$, $\sigma_m = 1.0$, $(R_\Delta^{-1})_{max} = 1.0$. (a) $t = 0$, (b) $t = 50$, (c) $t = 90$, (d) $t = 170$. Contours of the u velocity component.
——— 0.1, – – – – – 0.05, —— · —— 0.01, —— – —— -0.01, – – —— -0.05, ········· -0.1.
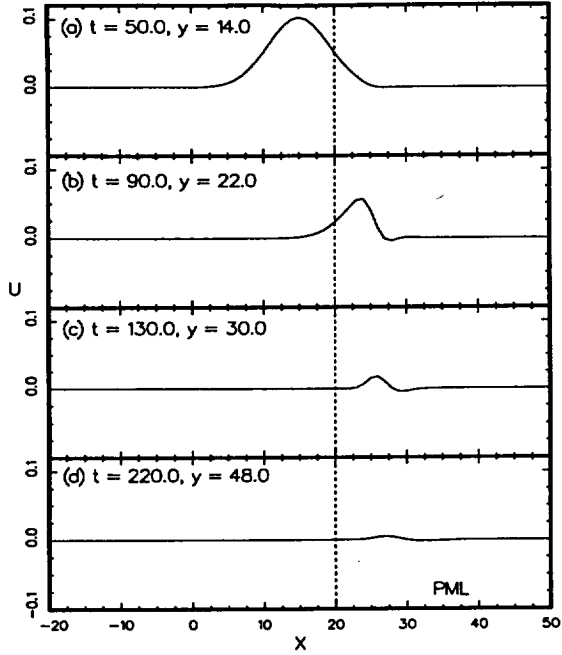
13

Figure 13. Waveforms showing the damping of a vorticity wave packet as it is convected into a PML with artificial selective damping terms. $M_x = 0.3$, $M_y = 0.2$, $\sigma_m = 1.0$, $(R_\Delta^{-1})_{max} = 1.0$.
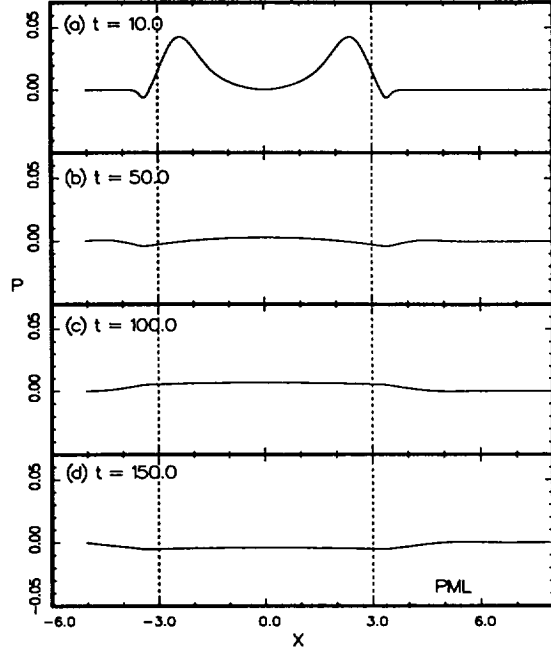

Figure 15. Pressure waveforms along the line $r = 0.38$ of a circular duct without mean flow showing the damping of an acoustic pulse in the PML. $\Delta x = \Delta r = \frac{R}{25}$, $\sigma_m = 25.0$.
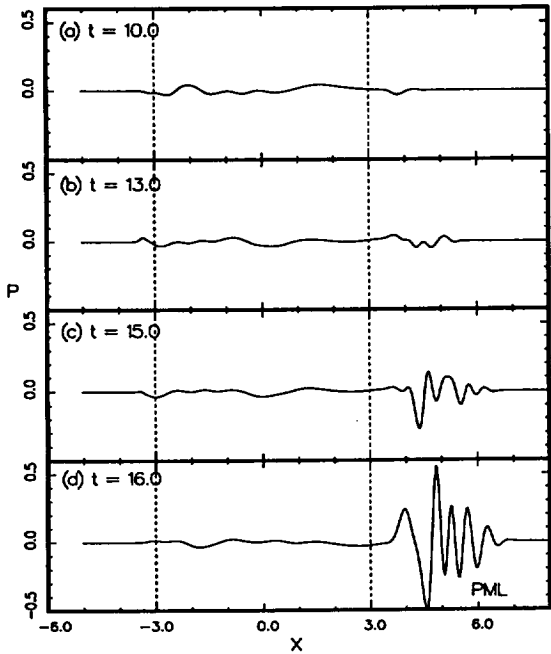

Figure 14. Pressure waveforms along the line $r = 0.38$ of a circular duct with uniform mean flow at Mach 0.4 showing the excitation and growth of the unstable solution in the PML by an acoustic pulse. $\Delta x = \Delta r = \frac{R}{25}$, $\sigma_m = 25.0$.

14

THE EFFECT OF NOZZLE GEOMETRY ON THE
NOISE OF HIGH-SPEED JETS

Christopher K.W. Tam

Department of Mathematics, Florida State University
Tallahassee, FL 32306-4510 USA

ABSTRACT

This paper examines the effectiveness of jet noise reduction by the use of different nozzle exit geometry. Since there will be thrust loss associated with a nozzle of complex geometry, consideration is confined to practical configurations with reasonably small thrust loss. In this study, only jets with a single stream are considered. The nozzle configurations examined are circular, elliptic and rectangular. Included also are plug nozzles as well as a suppressor nozzle. It is shown that the measured turbulent mixing noise of the jets from these nozzles consists of two independent components. The noise spectrum of each component is found to fit the shape of a seemingly universal similarity spectrum. It is also found that the maximum levels of the fitted noise power spectra of the jets are nearly the same. This finding suggests that nozzle geometry modification may not be an effective method for jet noise suppression.

1. INTRODUCTION

Reducing high-speed jet noise is currently a high priority research and development effort of the aircraft industry. Despite many years of jet noise research, noise reduction is a highly empirical endeavor. Since the early work of Westly and Lilley[1] many attempts have been made to modify the shape of the nozzle exit in the belief that this would reduce the turbulence intensity of the jet leading to a reduction in the radiated noise. On following this concept, plug nozzles, corrugated nozzles as well as nozzles with multi-chute elements have been introduced for noise suppression purpose.

The objective of this paper is to examine the effectiveness of jet noise reduction by nozzle exit geometry modification. Of course, there will be thrust loss in using a nozzle with complex geometry. Our consideration is, therefore, confined to practical geometries for which the thrust loss is reasonably small. In order to focus attention

on nozzle geometry alone, we will only consider jets formed by a single stream. Multi-stream jets, invariably, would introduce thermodynamic and other flow parameters as variables. Under this circumstance, a simple statement on the effectiveness of nozzle configuration for noise suppression cannot be easily made.

In Section 2 of this paper, the effect of nozzle geometry on the turbulent mixing processes in jets is discussed. For high-speed jets the mixing process is influenced only by upstream events. Thus the normal expectation is that the nozzle exit configuration would exert considerable influence on the development of the large and fine scale turbulence of the jet flow and hence its noise. In Section 3, turbulent mixing noise data from a variety of nozzles will be examined and analyzed. It will be shown that the noise level is, to a large extent, insensitive to the nozzle shape. This is true even for jets embedded in open wind tunnel flows simulating forward flight effects. This result seems to suggest that modification of a nozzle exit configuration may not be an effective method for noise suppression.

2. NOZZLE GEOMETRY AS AN INITIAL CONDITION

Tam and Chen[3], based on their observation of the noise directivity and spectrum measurements of Seiner *et al.*[4], were the first to clearly suggest that turbulent mixing noise from high-speed jets is made up of two components. One component is in the form of Mach wave radiation generated by the large turbulence structures of the jet flow. This component radiates only in the downstream direction. The other component is generated by the fine scale turbulence of the jet. The radiated noise has a more uniform directivity. Experimental confirmation of the existence of the two noise components was not available until the recent investigation of Tam, Golebiowski and Seiner[2]. By analyzing the entire data bank of axisymmetric jet noise spectra measured in the Jet Noise Laboratory of the NASA Langley Research Center, they were able to extract the shapes of two self-similar spectra from the data. They then demonstrated that all the noise spectra were made up of a combination of the two similarity spectra. Let S be the noise power spectrum (S has the dimensions of pressure squared per unit frequency) then S can be expressed in the following similarity form,

$$S = \left[AF\left(\frac{f}{f_L}\right) + BG\left(\frac{f}{f_F}\right) \right] \left(\frac{D_j}{r}\right)^2 \tag{1}$$

where $F\left(\frac{f}{f_L}\right)$ and $G\left(\frac{f}{f_F}\right)$ are the similarity spectra of the large turbulence structure noise and the fine scale turbulence noise respectively. f_L is the frequency at the peak of the large turbulence structures noise spectrum and f_F is the frequency at the peak of the fine scale turbulence noise spectrum. The spectrum functions are normalized such that $F(1) = G(1) = 1$. In equation (1), A and B are the amplitudes of the independent spectra. They have the same dimensions as S. D_j is the fully expanded jet diameter and r is the distance between the noise measurement point and the nozzle exit. The amplitudes A and B and the peak frequencies f_L and f_F are functions of the jet operating parameters $\frac{v_j}{a_\infty}$, $\frac{T_r}{T_\infty}$ and the direction of radiation χ (measured from the jet inlet). v_j and a_∞ are the jet velocity and the ambient sound speed. T_r and T_∞ are the reservoir and ambient temperature. One remarkable feature of the similarity spectra is that they fit the data well regardless of jet velocity, jet temperature, direction

of radiation, and whether the jet is perfectly or imperfectly expanded (in the case of supersonic jets). These spectra are used extensively in the present investigation.

In high-speed jet flows, there is practically very little upstream influence. Thus the turbulence level near the end of the core region, where most of the jet noise is generated, is affected primarily by the mixing processes upstream and the conditions at the nozzle exit. From this point of view, the nozzle geometry may be regarded as an initial condition on the spatial evolution of the jet velocity profile and the turbulence intensity and spectral content downstream. For noise suppression purposes, the crucial question to ask is how sensitive the turbulence level of the jet flow near the end of the potential core is to the initial condition at the nozzle exit. There is no question that by changing nozzle geometry the entrainment flow and hence jet turbulence in the region immediately downstream of the nozzle exit is affected. However, turbulent mixing is a highly nonlinear process. It is known, nonlinear process can lead to the same asymptotic state regardless of initial conditions. (For a discussion of the lack of influence of initial conditions on self-similar turbulent flows, see the work of Tam and Chen[5].) For high Reynolds number jet flows, it is possible that a jet issued from a noncircular nozzle evolves quickly into a more or less axisymmetric jet before the end of the core is reached. In such a case, the radiated noise would be similar to that of a circular jet both in intensity and spectral content. In the next section, it will be shown that this appears to be the case.

3. EVALUATION AND COMPARISONS OF DATA

Supersonic jet noise data from two sources are used in the present study. The first set of data is taken from the data bank of the Jet Noise Laboratory of the NASA Langley Research Center. This set of data consists of noise spectra from a Mach 2 aspect ratio 3 elliptic jet and a Mach 2 aspect ratio 7.6 rectangular jet. These are high quality data; comparable to those used in the work of Tam, Golebiowski and Seiner[2].

The second set of data is taken from the published measurements of Yamamoto et al.[6]. In this series of experiments, six nozzles are used. They include a conical nozzle, a convergent-divergent (C-D) round nozzle, a convergent annular plug nozzle, a C-D annular plug nozzle, a 20-chute annular plug suppressor nozzle with convergent flow segment terminations and a 20-chute annular plug suppressor nozzle with C-D flow element terminations. The noise spectra of the jet from the fifth nozzle, however, are strongly different from the same configuration suppressor nozzle but with C-D flow element terminations and the other nozzles. Without knowing the cause of the difference, it is decided to ignore the data associated with this nozzle.

3.1 COMPARISONS WITH SIMILARITY NOISE SPECTRA

Figure 1 shows direct comparisons between the measured elliptic and rectangular jet noise spectra at Mach 2 and $\frac{T_r}{T_\infty} = 1.8$ from the NASA Langley Research Center and the similarity spectrum for the large turbulence structures noise of Tam et al.[2] at $\chi = 150$ deg. The elliptic jet noise data are measured on three planes containing the jet axis. One is on the minor axis plane, one on a plane at 58 degrees to the minor axis plane and the third on the major axis plane. They are the top three curves in the figure. The bottom two curves are from the rectangular jet noise data measured on the minor and major axis planes. As can be seen, there is good agreement between the

measured spectrum shapes and the similarity noise spectrum (the $F(\frac{f}{f_L})$ function of equation (1)). This is so despite the fact that the nozzle geometries are very different.

Comparisons between the measured spectra at $\chi = 90$ deg. and the similarity noise spectrum or the fine scale turbulence noise (the $G(\frac{f}{f_F})$ function of equation (1)) for the elliptic and rectangular jets are given in Figure 2. Again, the top three curves are those of the elliptic jet and the bottom two curves are of the rectangular jet measured on the same azimuthal planes as in Figure 1. It is evident that there is good agreement overall regardless of nozzle shapes.

Figure 3 shows the noise spectrum shapes of the Yamamoto et al. data[6] at $\chi = 150$ deg. The jet velocity in each case is very close to 2420 ft/sec and the total temperature is approximately 1715 deg. Rankine. The four spectra are (from the top down) from the C-D round nozzle, the convergent annular plug nozzle, the C-D annular plug nozzle and the 20-chute annular suppressor nozzle. The data from the conical nozzle is nearly the same as the C-D round nozzle and is, therefore, not displayed. The full curves are the similarity noise spectrum (the $F(\frac{f}{f_L})$ function) of Tam et al.[2]. On ignoring the very low frequency part of the noise spectrum, it is clear that the agreement between the measured data and the similarity spectrum is good for all the cases.

Figure 4 shows similar comparisons as in Figure 3 but at $\chi = 90$ deg. By comparing the several spectra shown, the facility noise contamination at low frequencies can be readily detected. The full curves are the similarity spectrum given by the $G(\frac{f}{f_F})$ function. Overall, there is again good fit between the data and the similarity spectrum.

3.2 COMPARISONS OF MAXIMUM SOUND PRESSURE LEVELS

To assess whether nozzle geometry has significant influence on high-speed jet noise, we compare the sound pressure levels at the peaks of the fitted noise spectra, $SPL_{\max}$, in dB/Hz at $r = 100D_j$ from the various jets with the level of the simple circular C-D nozzle. The results are shown in Tables 1 to 4.

Table 1 compares the $SPL_{\max}$ of the elliptic jet at temperature ratio ($\frac{T_r}{T_\infty}$) of 1.0, 1.37, 1.80 and 2.27 at jet Mach number 1.98 with the corresponding values of a circular jet. We have chosen the microphone measurements at $\chi = 150$ deg. to characterize the large turbulence structures noise component and the microphone measurements at $\chi = 90$ deg. to characterize the fine scale turbulence noise component. The first row of data is measured in the minor axis plane. The second row is measured in a plane at 58 degrees to the minor axis plane. The third row is measured in the major axis plane. The last row is the data from a circular jet at the same jet velocity and total temperature. Within experimental uncertainty, it is clear from the table that the noise from the elliptic jet is, first of all, quite axisymmetric. Further, it is nearly the same as the circular jet. Table 2 provides direct comparisons between the $SPL_{\max}$ of the rectangular jet and a circular jet. Again, within experimental uncertainty, there is very little difference in the noise levels.

Tables 3 and 4 show the $SPL_{\max}$ data at $\chi = 150$ and 90 deg. for the various nozzles of the Yamamoto et al. experiments. It is worthwhile to remind the readers that the data are converted from $\frac{1}{3}$ octave band measurements and possibly slightly contaminated by shock and facility noise. The experimental uncertainty could be as large as 2 to 3 dB by our estimate. By comparing all the data with those of the C-D nozzle, it is evident that the differences are well within the experimental uncertainty. Thus, in spite of the large differences in nozzle geometry, the noise from supersonic jets

are remarkably the same. Based on these results, it is possible to surmise that nozzle exit geometry may not have significant control over the noise of high-speed jets.

4. CONCLUSION

Extensive comparisons between the noise radiated by supersonic jets operating at various temperatures and velocities with and without simulated forward flight and the noise from a circular jet at the same conditions have been carried out. Seven nozzles of practical geometries are included in the study. It is found that regardless of nozzle geometry, turbulent mixing noise of all the jets is comprised of two components. One component is the noise from the large turbulence structures and the other is noise from the fine scale turbulence of the jet flow. Further, the radiated sound is largely axisymmetric and that the shapes of the spectra of the two noise components are nearly the same as those of the similarity spectra of Tam, Golebiowski and Seiner[2]. In addition, the noise levels are essentially independent of nozzle configuration. Based on these results, it is concluded (bearing in mind the limited scope of this study) that nozzle geometry modification may not be an effective method for jet noise suppression.

ACKNOWLEDGMENT

Table 1. Elliptic jet (aspect ratio 3, $M_j = 1.98$)

	$\chi = 90$ deg.				$\chi = 141$ deg.				
T_r/T_∞	1.00	1.37	1.80	2.27	1.00	1.37	1.80	2.27	measurement plane
SPL_{max}	74.3	75.5	77.0		96.8	99.5	101.7		minor axis plane
at $r = 100D_j$	74.3	75.7	76.8	78.3	96.1	98.8	100.3	101.3	58 deg. plane
(dB/Hz)	74.5	75.5	77.0	78.6	94.4	97.5	101.7	101.7	major axis plane
	75.5	76.2	77.3	78.5	97.3	99.3	100.7	102.1	circular jet

Table 2. Rectangular jet (aspect ratio 7.6, $M_j = 2.0$)

	$\chi = 90$ deg.			$\chi = 150$ deg.			
T_r/T_∞	1.10	1.82	2.26	1.10	1.82	2.26	measurement plane
SPL_{max}	74.9	76.9	77.5	98.5	102.1	102.4	minor axis plane
at $r = 100D_j$	74.9	75.9	77.0	98.1	100.2	100.6	major axis plane
(dB/Hz)	76.0	77.7	78.8	98.4	101.5	102.6	circular jet

Table 3. Yamamoto *et al.* data
($v_j \simeq 2420$ ft/sec, $T_r \simeq 1715$ deg. R)

nozzle type	conical nozzle	C-D nozzle $M_d = 1.4$	convergent plug nozzle	C-D plug nozzle	suppressor nozzle	inlet angle χ, degree
SPL_{max} at	98.8	97.7	98.7	99.0	97.4	150
$r = 100D_j$ (dB/Hz)	77.6	75.0	76.6	77.2	74.5	90

Table 4. Yamamoto *et al.* data
($v_j \simeq 1720$ ft/sec, $T_r \simeq 870$ deg. R)

nozzle type	C-D nozzle $M_d = 1.4$	convergent plug nozzle	C-D plug nozzle	suppressor nozzle	inlet angle χ, degree
SPL_{max} at	95.0	96.2	97.1	92.5	150
$r = 100D_j$ (dB/Hz)	70.3	73.0	74.0	70.0	90

REFERENCES

[1] Westley, R. and Lilley, G.M., "An Investigation of the Noise Field from a Small Jet and Methods for Its Reduction," Report No. 53, College of Aeronautics, Cranfield (England), Jan. 1952.

[2] Tam, C.K.W., Golebiowski, M. and Seiner, J.M., "On the Two Components of Turbulent Mixing Noise from Supersonic Jets," AIAA Paper 96–1716, May 1996.

[3] Tam, C.K.W. and Chen, P., "Turbulent Mixing Noise from Supersonic Jets," AIAA Journal, vol. 32, Sept. 1994, pp. 1774–1780.

[4] Seiner, J.M., Ponton, M.K., Jansen, B.J. and Lagen, N.T., "The Effects of Temperature on Supersonic Jet Noise Emission," AIAA Paper 92–2046, May 1992.

[5] Tam, C.K.W. and Chen, K.C., "A Statistical Model of Turbulence in Two-Dimensional Mixing Layers," Journal Fluid Mechanics, vol. 92, part 2 1979, pp. 303–326.

[6] Yamamoto, K., Brausch, J.F., Janardan, B.A., Hoerst, D.J., Price, A.O., and Knott, P.R., "Experimental Investigation of Shock-Cell Noise Reduction for Single-Stream Nozzles in Simulated Flight," Comprehensive Data Report. Volume I. Test Nozzles and Acoustic Data, NACA CR–168234, May, 1984.

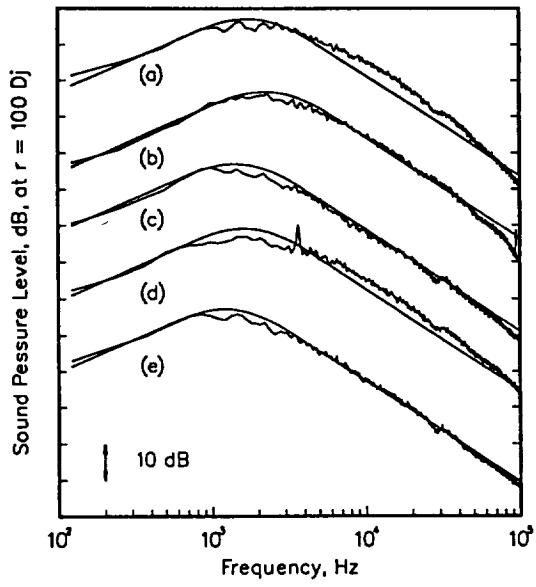[7] Tam, C.K.W., "Supersonic Jet Noise," Annual Review Fluid Mechanics, vol. 27, 1995, pp. 17–43.

Figure 1. Comparisons between elliptic and rectangular jet noise
data and the similarity spectrum at $\chi = 150$ deg., $\frac{T_r}{T_\infty} = 1.8$

Aspect ratio 3 elliptic jet: (a) minor axis plane, (b) 58 degree
plane, (c) major axis plane.

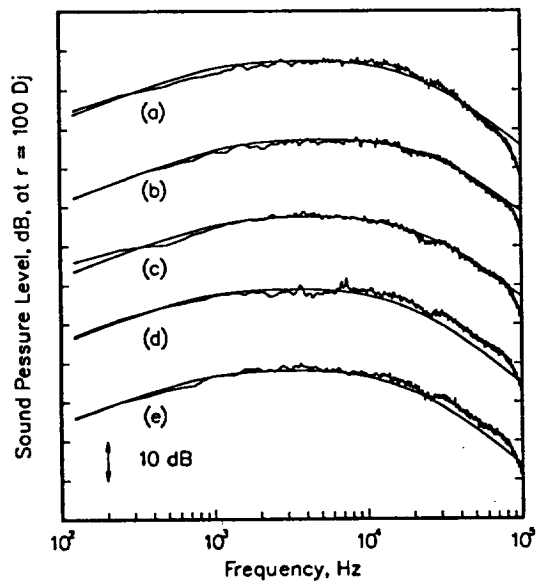Aspect ratio 7.6 rectangular jet: (d) minor, (e) major axis plane.

Figure 2. Comparisons between elliptic and rectangular jet noise
data and the similarity spectrum at $\chi = 90$deg., $\frac{T_r}{T_\infty} = 1.8$

Aspect ratio 3 elliptic jet: (a) minor axis plane, (b) 58 degree
pla ne, (c) major axis plane.

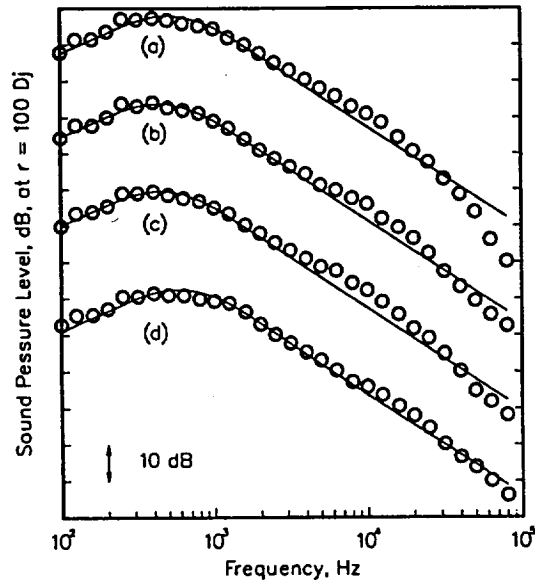Aspect ratio 7.6 rectangular jet: (d) minor, (e) major axis plane.

Figure 3. Comparisons between Yamamoto *et al.* data and the similarity spectrum. $V_j \simeq 2420$ ft/sec, $T_r \simeq 1715$ deg R, $\chi = 150$ deg; o data, ——— similarity spectrum. (a) C-D nozzle, (b) convergent plug nozzle, (c) C-D plug nozzle, (d) 20-chute C-D suppressor nozzle.
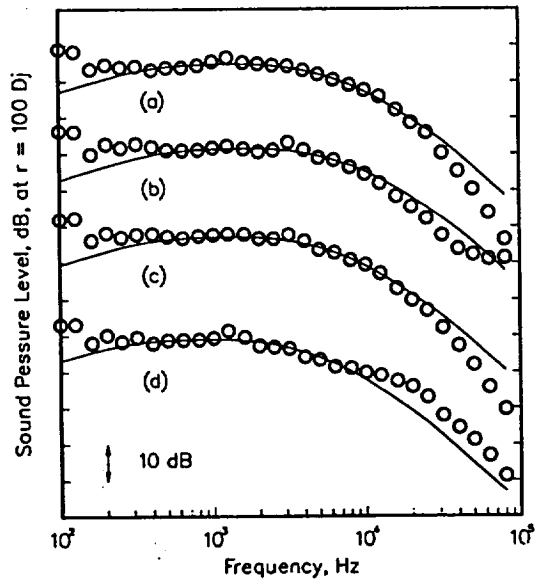

Figure 4. Comparisons between Yamamoto *et al.* data and the similarity spectrum. $V_j \simeq 2420$ ft/sec, $T_r \simeq 1715$ deg R, $\chi = 90$ deg; o data, ——— similarity spectrum. (a) C-D nozzle, (b) convergent plug nozzle, (c) C-D plug nozzle, (d) 20-chute C-D suppressor nozzle.